



Humidified single-scattering albedometer (H-CAPS-PM_{SSA}): Design, data analysis, and validation

Christian M. Carrico, Tyler J. Capek, Kyle J. Gorkowski, Jared T. Lam, Sabina Gulick, Jaimy Karacaoglu, James E. Lee, Charlotte Dungan, Allison C. Aiken, Timothy B. Onasch, Andrew Freedman, Claudio Mazzoleni & Manvendra K. Dubey

To cite this article: Christian M. Carrico, Tyler J. Capek, Kyle J. Gorkowski, Jared T. Lam, Sabina Gulick, Jaimy Karacaoglu, James E. Lee, Charlotte Dungan, Allison C. Aiken, Timothy B. Onasch, Andrew Freedman, Claudio Mazzoleni & Manvendra K. Dubey (2021): Humidified single-scattering albedometer (H-CAPS-PM_{SSA}): Design, data analysis, and validation, *Aerosol Science and Technology*, DOI: [10.1080/02786826.2021.1895430](https://doi.org/10.1080/02786826.2021.1895430)

To link to this article: <https://doi.org/10.1080/02786826.2021.1895430>



Published online: 23 Mar 2021.



Submit your article to this journal [↗](#)



Article views: 43



View related articles [↗](#)



View Crossmark data [↗](#)



Humidified single-scattering albedometer (H-CAPS-PM_{SSA}): Design, data analysis, and validation

Christian M. Carrico^a , Tyler J. Capek^{b,c} , Kyle J. Gorkowski^c , Jared T. Lam^{a,c} , Sabina Gulick^{a,c} , Jaimy Karacaoglu^a , James E. Lee^c , Charlotte Dungan^a , Allison C. Aiken^c , Timothy B. Onasch^d , Andrew Freedman^d , Claudio Mazzoleni^b , and Manvendra K. Dubey^c

^aDepartment of Civil and Environmental Engineering, New Mexico Institute of Mining and Technology, Socorro, New Mexico, USA; ^bPhysics Department, Michigan Technological University, Houghton, Michigan, USA; ^cEarth and Environmental Sciences (EES-14), Los Alamos National Laboratory, Los Alamos, New Mexico, USA; ^dAerodyne Research, Inc., Billerica, Massachusetts, USA

ABSTRACT

We report the development and validation of a new humidified aerosol single-scattering albedometer to quantify the effects of water uptake on submicrometer particle optical properties. The instrument simultaneously measures in situ aerosol light extinction (σ_{ep}) and scattering (σ_{sp}) using a cavity-attenuated phase shift-single scattering albedo particulate matter (PM) monitor (CAPS-PM_{SSA}, Aerodyne Research, Inc., Billerica, MA, USA). It retrieves by difference aerosol light absorption (σ_{ap}) and directly quantifies aerosol single-scattering albedo (SSA), the aerosol “brightness.” We custom built a relative humidity (RH) control system using a water vapor-permeable membrane humidifier and coupled it to the CAPS-PM_{SSA} to enable humidified aerosol observations. Our humidified instrument (H-CAPS-PM_{SSA}) overcomes problems with noise caused by mirror purge-flow humidification, heating, and characterizing cell RH. Careful angular truncation corrections in scattering, particularly for larger particles, were combined with empirical observations. Results show that the optimal operational size to be $D_p < 400$ nm. The H-CAPS-PM_{SSA} was evaluated with several pure single-component aerosols including ammonium sulfate ((NH₄)₂SO₄), absorbing nigrosin, and levoglucosan, an organic biomass smoke tracer. The measured σ_{ep} , σ_{sp} , and the derived optical hygroscopicity parameter (κ) for size-selected ammonium sulfate are in good agreement with literature values. For dry size-selected nigrosin in the $100 < D_p < 400$ nm range, SSA values increased from ~ 0.3 to 0.65 with increasing D_p . The enhancement in nigrosin σ_{ap} at RH = 80% was a factor of 1.05–1.20 relative to dry conditions, with the larger particles showing greater enhancement. SSA increased with RH with the largest fractional enhancement measured for the smallest particles. For polydisperse levoglucosan, we measured an optical κ of 0.26 for both light extinction and scattering and negligible absorption. Our new instrument enables reliable observations of the effects of ambient humidity on mixed aerosol optical properties, particularly for light-absorbing aerosols whose climate forcing is uncertain due to measurement gaps.

ARTICLE HISTORY

Received 4 October 2020
Accepted 10 February 2021

EDITOR

Nicole Riemer

1. Introduction

Atmospheric aerosols have important effects on human health, regional haze, and climate forcing. The latter includes both a direct effect (Yu et al. 2006) via light extinction, and indirect effects on cloud formation, properties, and lifetime for both liquid and ice clouds (DeMott et al. 2010; Lohmann and Feichter 2005). Light extinction by particles at a given wavelength (λ), quantified as an extinction coefficient (σ_{ep} with dimensions of inverse length), is the sum of light scattering (σ_{sp}) and light absorption (σ_{ap}) by particles.

The magnitudes and uncertainties of σ_{ep} , σ_{sp} , and σ_{ap} are critical for climate impact assessments. In particular, complex aerosol physicochemical properties, their heterogeneity in time and space, and the interplay between their light scattering and absorbing properties demand intensive research.

1.1. Measurements of particle light scattering dependence on relative humidity

Relative humidity (RH, %) affects aerosol water content, and therefore optical properties and climate

CONTACT C. M. Carrico carrico@nmt.edu Department of Civil and Environmental Engineering, New Mexico Institute of Mining and Technology, Socorro, NM 87801, USA; M. K. Dubey dubey@lanl.gov Earth and Environmental Sciences (EES-14), Los Alamos National Laboratory, Los Alamos, NM 87545, USA.

(Seinfeld and Pandis 1998). These effects have been measured by nephelometry and other techniques since the 1970s (Anderson and Ogren 1998; Heintzenberg et al. 2006; Tang et al. 2019). Aerosol composition is critical for RH effects, as, primary soot carbon aerosols are generally considered hydrophobic (Bond and Bergstrom 2006), whereas inorganics such as ammonium sulfate $[(\text{NH}_4)_2\text{SO}_4]$ are hydrophilic (Xu and Penner 2012). Fresh hydrophobic soot and organic aerosols are oxidized with age and mix with hydrophilic components enhancing water uptake. As particles grow with RH, the aerosol lifetime, particle cross-sectional area, volume, composition, and refractive index change. Competing effects of humidity on σ_{ap} include amplification by lensing effects, reduction by compaction (China et al. 2013), and larger scattering. Lacking humidity-dependent observations, particularly for light-absorbing aerosols, aerosol representations in models have large uncertainties (Cappa et al. 2012; Matsui, Hamilton and Mahowald 2018; Wang et al. 2018).

A common intensive parameter is the light scattering hygroscopic growth factor, $f(\text{RH})$, that is the ratio of σ_{sp} at a given λ at high RH (typically $\text{RH} > 80\%$) to that at $\text{RH} < 40\%$, also defined similarly for σ_{ep} or σ_{ap} (Equation (1))

$$f(\text{RH}) = \frac{\sigma_{\text{sp}, \lambda, \text{RHhigh}}}{\sigma_{\text{sp}, \lambda, \text{RHlow}}} \quad (1)$$

Petters and Kreidenweis (2007) developed a single κ -parameter model of particle diameter (D_p) hygroscopic growth factors (D/D_0). This was extended to light extinction relating $f(\text{RH})$ to an optical hygroscopicity (κ_{ep}) parameter (Brock, Wagner, Anderson, Attwood et al. 2016; Brock, Wagner, Anderson, Beyersdorf et al. 2016), and defined similarly for κ_{sp} and κ_{ap} with several simplifying assumptions (Equation (2)). To approximate and compare hygroscopicity for different aerosol compositions, we use the “optical κ ” metric with ep, sp, ap subscripts as appropriate, and distinguish it from the κ -parameter for D/D_0 .

$$\kappa_{\text{ep}} = \left(f(\text{RH})_{\text{ep}} - 1 \right) \times \frac{100 - \text{RH}}{\text{RH}} \quad (2)$$

In general, hygroscopicity decreases with increasing aerosol carbonaceous fraction in biomass burning aerosols (Carrico et al. 2005; Malm et al. 2005) and ambient aerosols (Orozco et al. 2016; Quinn et al. 2005). However, this decrease depends on carbonaceous speciation and aging.

1.2. Measurement of RH dependence of spectrally resolved light absorption

The climatic importance of light-absorbing mixed carbonaceous aerosols and their hygroscopicity are

well-recognized and depend on their composition, mixing state, and morphology (Bond et al. 2013). “Black carbon” (BC) or “soot” particles form fractal-like agglomerates of refractory carbon spherules ($D_p \sim 20 \text{ nm}$). Although fresh BC is hydrophobic, oxidation and mixing with inorganics both increase hygroscopicity over time (Zhang et al. 2020).

Biomass burning emits and leads to secondary formation of less refractory “brown carbon” (BrC) with stronger absorption in the blue and UV than BC (Lack et al. 2012; Lee et al. 2020). BrC is a key absorbing species whose RH dependence is poorly characterized (Washenfelder et al. 2015). A lensing effect of mixed BC–BrC aerosols can shift a net cooling to net warming with BrC (Saleh et al. 2013, 2014). Furthermore, BrC evolves as it is transported downwind where oxidization can lead to bleaching (Forrister et al. 2015) while cloud processing can produce additional BrC. Oxidation also increases BrC aerosol polarity and thus hygroscopicity (Duplissy et al. 2011; Gorkowski, Preston, and Zuend 2019).

Common absorption techniques, such as the multi-wavelength aethalometer and the particle soot absorption photometer (PSAP), measure filter deposits rather than *in situ* aerosol (Cross et al. 2010). Filter absorption overestimates result from imperfect scattering corrections (Bond, Anderson and Campbell 1999; Drinovec et al. 2015) and organics modifying the substrate optical properties (Cappa et al. 2008). Several correction schemes, including shadowing and multiple scattering in the filter matrix, have been applied to dry aerosols (Coen et al. 2010; Petzold et al. 2013). Due to filter effects on water uptake, the aethalometer is poorly suited to RH studies (Arnott et al. 2003). Other direct *in situ* techniques (e.g., photoacoustic and photothermal) are also subject to interferences at higher RH ($>30\%$) due to evaporation limiting their utility (Diveky et al. 2019; Lewis et al. 2009).

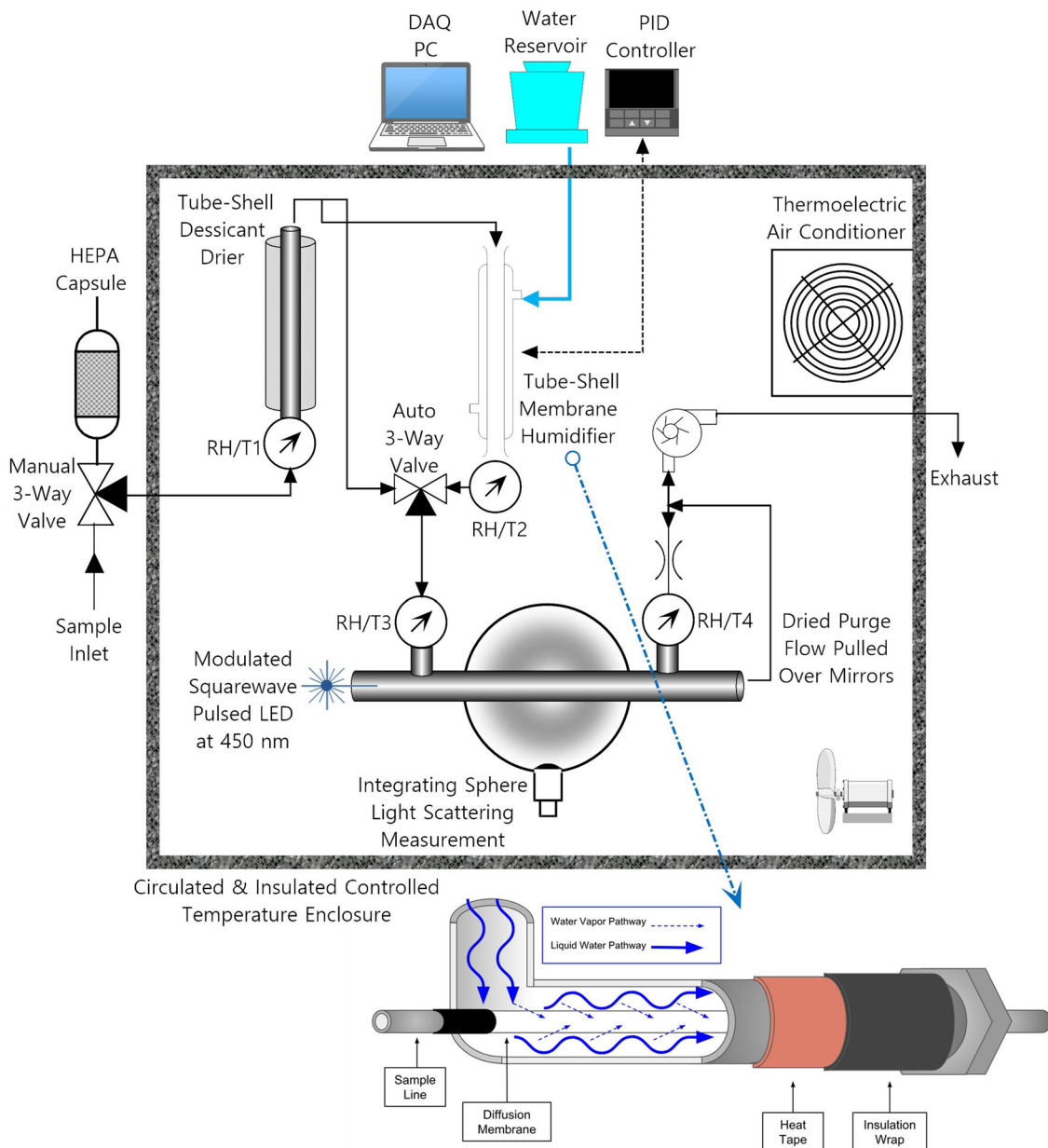
The single-scattering albedo (SSA) quantifies the relative importance of σ_{sp} at a given wavelength, λ and depends on RH (Equation (3)). SSA determines in part whether a given aerosol warms or cools climate (Russell et al. 2002). Observations of $\text{SSA}(\lambda, \text{RH})$ are critical to quantify the net climate forcing as σ_{sp} and σ_{ap} have different κ .

$$\text{SSA}(\lambda, \text{RH}) = \frac{\sigma_{\text{sp}, \lambda, \text{RH}}}{\sigma_{\text{ep}, \lambda, \text{RH}}} \quad (3)$$

Previous studies of RH-dependent optical properties have simplistically assumed constant $\sigma_{\text{ap}}(\text{RH})$ (Carrico et al. 2003). Accurate measurements of the RH dependence of σ_{ap} and SSA are needed to

Table 1. Summary of studies relevant to absorbing aerosols, aerosol single scattering albedo, and relative humidity (RH) dependence.

Study	Technique	Measured parameters	Wavelength(s) (nm)	Measured RH dependence?
Garland et al. (2007)	Cavity Ring Down Spectrometer (CRDS)	σ_{ep}	532	Yes
Baynard et al. (2007)	CRDS	σ_{ep}	355, 532, 683, 1064	Yes
Langridge et al. (2011)	CRDS	σ_{ep}	405, 532, 662	Yes
Zhao et al. (2017)	Broadband Cavity Enhanced Aerosol Extinction Spectrometry	σ_{ep}	461	Yes
Massoli et al. (2009)	CRDS + Photoacoustic Spectrometer	σ_{ep}	355, 532, 1064	Yes
Carrico et al. (2003)	Particle Soot Absorption Photometer + Nephelometer	σ_{ap}	565	No
		σ_{sp}	450, 550, 700	Yes
		SSA	550	In part
Zhou et al. (2020)	Cavity Enhanced Albedometer	σ_{ep} , σ_{spr} , SSA	532	Yes
Brem et al. (2012)	Short-Path Extinction Cell Nephelometer	σ_{ep} , σ_{sp}	467, 530, 660	Yes
Michel Flores et al. (2012)	CRDS	σ_{ep}	355, 532	Yes
This study	Cavity Attenuated Phase Shift (CAPS)	σ_{ep} , σ_{spr} , SSA	450	Yes

**Figure 1.** Experimental flow diagram showing RH controlled cavity attenuated phase shift instrument (H-CAPS-PM_{SSA}). Lower detail shows the interior of the humidifier consisting of a liquid water jacket surrounding the interior aerosol sample flow. Water jacket and aerosol flow are separated by a semi-rigid water-vapor permeable membrane.

quantify direct and semi-direct (e.g., cloud evaporation by aerosol light absorption) climate forcing of aerosols.

1.3. Evolution of humidity-dependent aerosol optical property instrumentation

Beyond nephelometry, several RH-controlled techniques exist. Traditional light extinction methods rely on long, open-path, instruments with low sensitivity or are ill-suited for *in situ* process studies (Gordon et al. 2018; Malm and Persha 1991). Several instruments have measured λ -dependent light extinction *in situ* including the cavity ring-down spectrometer (CRDS) (Baynard et al. 2007; Langridge et al. 2011; Washenfelder et al. 2013). Using cavity ring-down spectroscopy, Baynard et al. (2006) and Langridge et al. (2011) explored hygroscopicity and light extinction of inorganic–organic mixtures and ambient aerosols. Recent studies used a cavity-enhanced albedometer at $\lambda = 532$ nm, similar to our instrument, to measure the RH dependence of light extinction and scattering by mixing dry and humid flows (Zhou et al. 2019, 2020; Zhao et al. 2017). These studies used truncation reduction tubes to limit angular truncation losses, but size-dependent truncation corrections were not explored (Zhou et al. 2020).

Other advanced σ_{ap} techniques rely on photoacoustic spectroscopy (PAS) which is limited to dry aerosols due to laser heating (Arnott et al. 1999, 2003; Flowers et al. 2010). This heating affects the dynamic partitioning of water and was first identified by Arnott et al. (2003), measured *in situ* by Lewis et al. (2009), and quantified as a function of particle size later (Diveky et al. 2019). Langridge et al. (2011) showed that nonlinearities in PAS signals limit the use to low RH. Combinations of multiple optical instruments have probed RH dependence, though often on different sample flows or differing λ .

The cavity-attenuated phase shift particulate matter extinction instrument (CAPS-PM_{ex}) originally measured only σ_{ep} . To quantify SSA, past measurements used a combination of instruments, for example, CRD spectroscopy and nephelometry (Singh, Fiddler, and Bililign 2016). The cavity-attenuated phase shift particulate matter-single scattering albedo (CAPS-PM_{SSA}) monitor measures both light extinction and light scattering simultaneously for the same aerosol volume (Onasch et al. 2015). We summarize the SSA and absorption techniques, their applicability or limitations for RH dependence measurements, and other key features in Table 1.

2. Measurement system details

2.1. CAPS-PM_{ex} and CAPS-PM_{SSA} instruments

We report here the development, calibration, and evaluation of a novel humidity-controlled cavity-attenuated phase shift particulate matter albedometer (H-CAPS-PM_{SSA}). The CAPS-PM_{SSA} instrument at the heart of this measurement system, is a recent, commercial *in situ* flow-through optical instrument at a discrete λ (Onasch et al. 2015). The basic instrument geometry is illustrated in our system design diagram in Figure 1, and its design and performance are detailed in the work by Onasch et al., (2015) and references therein. It simultaneously measures σ_{sp} and σ_{ep} in the same volume and hence aerosol SSA and σ_{ap} . The humidity-controlled H-CAPS-PM_{SSA} instrument is based on the design of a dual-nephelometer $f(\text{RH})$ light scattering system (Carrico et al. 2018; Gomez et al. 2018) that was modified for use a single CAPS-PM_{SSA} instrument as described below.

The original CAPS-PM_{ex} instrument measures light extinction only and reduces the detection threshold and path length constraints with an *in situ* light-emitting diode (LED) phase-shift method. It uses light reflection off of mirrors at the ends of a ~ 0.2 m physical cavity (Freedman 2014). The CAPS-PM_{ex} optical cell is fitted with high-reflectivity mirrors ($R \geq 0.9998$) at each end. This configuration gives it an effective path length of ~ 2 km with repeated reflections. Thus it can measure with a lower detection limit (LDL) of 2 Mm^{-1} at 1 s, or less at longer time-scales (Kebabian, Robinson and Freedman 2007; Massoli et al. 2010). Massoli et al. (2010) found similar performance with extinction precision of $\pm 3\%$ for pure scattering aerosols that agrees with Mie modeling within the 10% uncertainty in particle counting and a $3\text{-}\sigma$ detection limit of 3 Mm^{-1} at 1-s. The LED light source outputs a modulated square wave that is transmitted through the input mirror into the cavity. The light leaks through the output mirror and reaches a large vacuum photodiode (LVPD) detector. A phase shift of the light occurs over the folded light path that is proportional to the light extinction as well as the known cell geometry (Onasch et al. 2015).

The CAPS-PM_{SSA} also incorporates a Lambertian integrating sphere nephelometer to maximize scattered light collection within a standard extinction cell of the CAPS-PM_{ex}. The scattering channel uses a photomultiplier tube (PMT) detector perpendicular to the sample cell that is activated only when the LEDs are switched off, and thus the PMTs only measure the light scattered by aerosols inside the sample cell.

Pressure and temperature sensors allow correction and subtraction for real-time changes in air Rayleigh scattering. A comparison of CAPS-PM_{ex} with a nephelometer plus PSAP showed linear relationships with actual light extinction for many aerosol types (Petzold et al. 2013).

The CAPS-PM_{SSA} instrument measures σ_{ep} and σ_{sp} in a common sample volume at a discrete λ determined by the LED (Onasch et al. 2015). Our instrument uses $\lambda = 450$ nm with a 20 nm bandwidth (Kebabian, Robinson, and Freedman 2007). This exploits the larger scattering and absorption signals at shorter λ , reduced water vapor absorption, and allows probing of brown carbon properties at short wavelength. The scattering channel is calibrated to the extinction using a non-absorbing aerosol (Onasch et al. 2015). CAPS-PM_{SSA} scattering and extinction yield precise estimates of SSA as their ratio and sensitive estimates of absorption as the difference between them (Onasch et al. 2015). The result is a measurement of SSA to within 5%–10% based on extensive field testing (Modini et al. 2020). SSA approaches one for a negligible absorber (e.g., ammonium sulfate and polystyrene latex spheres or PSLs) while decreasing toward zero for a strong absorber like soot. With increasing SSA, the uncertainty in σ_{ap} increases as it is a small difference between two large signals. At SSA ~ 0.05 , the CAPS-PM_{ex} has an accuracy of 5% for σ_{ap} . However, at SSA ~ 0.50 , the uncertainty in σ_{ap} is $\sim 13\%$ and increases to above 60% for SSA values larger than 0.95 (Onasch et al. 2015). A comparison of SSA from the CAPS-PM_{SSA} with the CAPS-PM_{ex} plus aethalometer diverged at low SSA, attributable to an absorption bias in the aethalometer (Han et al. 2017). Much of the uncertainty for low SSA aerosols relates to the absorption efficiency of coated soot spheres and modeling of core-shell versus uniform absorbers in filter-based studies (Brem et al. 2012).

The CAPS-PM_{SSA} has a small angular cone in the forward and backscatter directions where scattered light escapes the cell. This angular truncation is independent of absorption but depends on the scattering phase function and requires corrections (Liu et al. 2018). The open tube ends cause minor angular truncation and together with the 98% reflectivity of the integrating sphere cause a low bias in light scattering (Han et al. 2017). Onasch et al. (2015) corrected for the CAPS truncation that increases with particle size. Several studies have examined and developed truncation correction schemes (de Faria et al. 2017; Liu et al. 2018; Modini et al. 2021). The CAPS technique also requires a geometry factor correction to

compensate for signal distortion in the photodetectors by the purge flows in the cell's mirrors (Onasch et al. 2015). The CAPS-PM_{ex} monitor uses a geometry correction factor of 1.27, while the CAPS-PM_{SSA} monitor uses a correction factor of 1.37 (due to a slightly shorter pathlength). We carefully implement and evaluate these corrections in our algorithms and perform experiments on size selected pure aerosols whose optical properties and water uptake are well known to calibrate the system.

2.2. Humidified CAPS-PM_{SSA} measurement system design details

We integrated the CAPS-PM_{SSA} instrument into a measurement system that includes external RH/temperature (RH/T) sensors, temperature control, and a humidification system including an electronically actuated three-way valve to select the dry or humid lines using a single CAPS-PM_{SSA} instrument (Figure 1). At the system inlet, a manual stainless steel three-way ball valve allows aerosol sampling as well as zero checks with a HEPA filter (Pall-Gelman Science, Inc., Port Washington, NY, USA, Model No. 12144 or similar). Tubing for plumbing is copper (6.4 mm OD) unless otherwise noted and connections are made with stainless steel or brass tube fittings (Swagelok, Inc., Solon, OH, USA, or similar). Next, the sample is dried in a concentric screened dryer (Droplet Measurement Technologies, Inc., Boulder, CO, USA, ASSY-1110) using a desiccant in the outer shell (Teledyne, Xenia, OH, USA, calcium sulfate DrieRite or similar). Desiccant driers have been shown to remove more than water vapor in ambient studies (El-Sayed et al. 2016). The compounds ammonium sulfate and levoglucosan used have extremely low vapor pressures (< 24 μ Pa at 25 °C), and nigrosin is a large molecule that is expected to be nonvolatile. Although evaporating droplets have been demonstrated to lead to some BrC formation in lab studies (Lee et al. 2013), they are unlikely to occur in our single-component systems.

Since we currently use a single CAPS-PM_{SSA} instrument, switching between dry and humidified lines is necessary. Control of a large diameter electrically actuated three-way ball-valve (S&K Automation, Brescia, Italy, Valbia 8E069-VB015-302-1/2) switches between sample flow through the low RH non-humidified pathway, or flow through a humidifier (Figure 1). Positive DC polarity is used to switch the valve in one direction, and a relay switching module (Altronix, Inc., Brooklyn, NY, USA, 12VDC) is required to toggle the DC polarity to return the valve.

Valve switching is triggered by solid-state relays (Crouzet, Allen, TX, USA, 84137240, 100A or similar) and controlled by custom software (National Instruments, Inc., Austin, TX, USA, LabVIEW). By adding a second CAPS-PM_{SSA} instrument measuring dry continuously and synchronously, the switching would not be necessary.

A detailed schematic (Figure 1) also shows the interior construction of the cylindrical profile tube-shell rigid-membrane flow-through humidifier. The humidifier is housed in a $\frac{3}{4}$ " outer diameter stainless-steel shell approximately 35 cm in length. Aerosol flows along an interior $\frac{1}{4}$ " ID water vapor-permeable membrane (Microdyn-Nadir V8) that extends concentrically through the middle section of the outer shell. The inner tubular membrane is water vapor-permeable and semi-rigid (and thus self-supporting). It is sealed with silicone and heat-shrink tubing at each end where it connects to the system plumbing. A ~ 15 cm segment of membrane thus separates the aerosol flow and liquid water jacket that fills the annular space of the outer shell. A downstream vacuum pump pulls aerosol flow down the length of the membrane interior. The outer shell is wrapped by an insulated electrical heat tape with a variable voltage control (Omega Engineering, Inc., Norwalk, CT, USA, SRT051), and the heat tape is covered with insulation (Design Engineering, Inc., Avon Lake, OH, USA, 10005). The rate of humidification is determined by the rate of heating of the water jacket which is controlled by a PID controller (Electro-tech Systems, Inc., Perkasi, PA, USA, Model 5100) interfaced to a capacitive RH sensor (Rotronic, Inc., Hauppauge, NY, USA, Hygroclip) downstream of the humidifier (Figure 1). Downstream of the electrically actuated ball valve is a stainless-steel condensation trap. The internal coalescing filter was removed from the water trap to minimize aerosol losses.

RH/temperature sensors (E + E Elektronik, Inc., Engerwitzdorf, Austria, Model EE08) are placed in strategic locations and monitored at ~ 0.2 Hz (Figure 1). Sensors are thin-film flat plate capacitors and newly certified using the manufacturer 2-point calibration. Per the manufacturer, the stated RH uncertainty is $\pm 2\%$ at low RH and $\pm 3\%$ at $\text{RH} \geq 90\%$. Time response (τ_{90}) is 6 s, like other capacitive sensors, and temperature uncertainty is ± 0.2 °C (Pt-1000 sensor). Several iterations determined that the locations for the sensors most representative of the optical cell conditions were immediately upstream and downstream of the CAPS cell, with insulated plumbing between the sensor and the CAPS. The plumbing is

insulated between these points and the CAPS cell to help keep it isothermal, and RH response is discussed later.

The CAPS diaphragm pump drives the sample flow at a nominal rate of ~ 0.85 actual liters per minute (alpm) using the manufacturer-supplied orifice. Here the, flow rate was increased to ~ 1.8 alpm using a larger orifice to allow quicker time response with changing RH conditions. With a controlled flow rate of 1.8 alpm and a sample volume downstream of the humidifier of ~ 0.25 L, the plug-flow residence time is approximately 8 s upstream of the CAPS-PM_{SSA}. The CAPS-PM_{SSA} diverts and filters a portion of its sample flow (< 0.01 lpm) to purge the mirrors to prevent aerosol deposition and degradation of mirror reflectivity. Testing showed that a humidified purge flow caused variability in mirror reflectivity, introducing errors. The mirror purge was diverted through a membrane drier (Permapure, Inc., Lakewood, NJ, USA, MD-110-48S-4) to minimize this artifact. The pump was relocated outside the CAPS box to reduce heat loads in the instrument (with the lid removed to aid isothermal conditions). Upon exiting, the sample is filtered and vented.

The system is installed in a 0.91 m $H \times 0.61$ m $W \times 0.76$ m D rack-mountable temperature-controlled enclosure (EIC solutions Inc., Warminster, PA, USA Protector Series NEMA) with a solid-state thermoelectric air conditioner/heater (ThermoTEC Series, NEMA 4X, 800 BTU/h) controlled via a thermocouple and PID controller. Several small fans are operated inside the enclosure to enhance temperature uniformity and prevent potential cool spots and condensation.

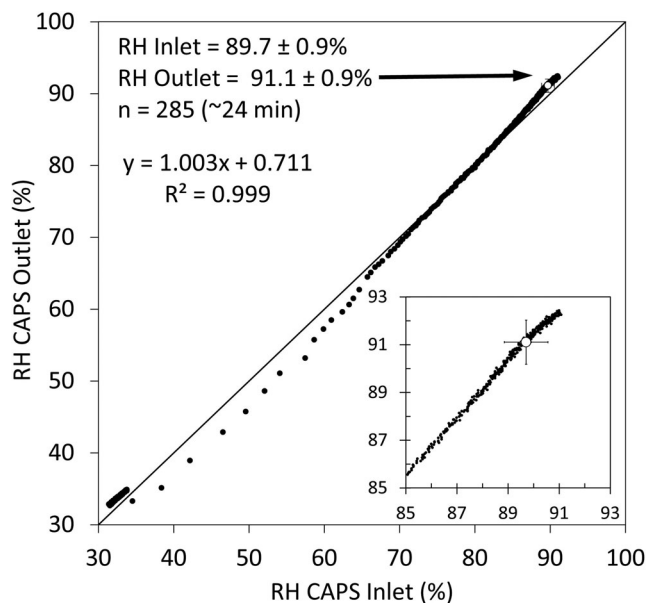
The entire system is controlled via a National Instruments LabVIEW virtual instrument (VI) that records light scattering coefficient, light extinction coefficient, instrument loss (a diagnostic indicating mirror cleanliness), temperature, and pressure measurements from the CAPS-PM_{SSA} and controls valve switching. Manufacturer-provided software is used for diagnostics and calibrating light scattering to extinction using a purely scattering aerosol.

2.3. H-CAPS-PM_{SSA} system characterization

Table 2 compares the sample thermal profile through the system when the sample flows through the dry and humid pathways. The nominal setpoint of the thermoelectric air conditioner is 25 °C to adjust sample conditions based on room temperature variations between ~ 20 and 30 °C. The sample enters the enclosure at room temperature and generally $\text{RH} < 20\%$.

Table 2. Typical profile of RH and temperature through H-CAPS-PM_{SSA} system (arithmetic means and standard deviations of 5-s data averaged over 42 RH scans, $n = 22,735$).

	T_1 (°C) Inlet	T_2 (°C) Humidifier	T_3 (°C) CAPS inlet	T_4 (°C) CAPS outlet	ΔT_{3-4} (°C) Across cell	ΔRH_{3-4} (%) Across cell
Low RH pathway						
Mean	22.81	25.54	24.58	24.64	0.06	0.85
StDev	0.26	0.14	0.22	0.19	0.10	0.96
High RH pathway						
Mean	22.77	25.60	24.53	24.67	0.14	-1.11
StDev	0.23	0.14	0.21	0.18	0.11	0.58

**Figure 2.** RH during an RH scan upward as measured immediately upstream and downstream of the CAPS optical cell.

Efforts are made to keep the sample isothermal through the system and limit the sample heating, though some warming does occur due to the humidifier, CAPS-PM_{SSA}, and other incidental electronics heat generation. The sample ΔT is limited to approximately 0.1 °C of heating across the CAPS cell resulting in ΔRH of -1%, below the uncertainty of the RH sensors.

While humidifying, the sample exits the humidifier at $40\% < RH < 95\%$ and then is transported into the sample cell. Due to slight warming into the CAPS, the RH in the cell is varied from the low value to up to $RH \sim 90\%$ (Figure 2). Agreement of upstream and downstream RH probes is shown to be within measurement uncertainties (Figure 2 and Table 2). Warming is due to a combination of residual system heat causing gradients, particularly while humidifying (Table 2).

A representative plot of CAPS RH upstream and downstream of the cell as measured with the capacitive RH sensors is shown in Figure 2. The mean and standard deviation of the absolute difference between the two sensors during an RH scan is $0.9 \pm 1.0\%$ in RH percent; the downstream sensor lags the upstream

Table 3. Comparison of light extinction, scattering and absorption coefficients (σ_{ep} , σ_{sp} , and σ_{ap} , respectively) at $\lambda = 450$ nm of filtered air at low and high RH ($n = 297$, 5-s data).

(1/Mm)	RH < 20%		
	σ_{ep}	σ_{sp}	σ_{ap}
Mean	-0.06	0.52	-0.58
StDev	0.91	0.83	1.16
(1/Mm)	RH = 80%		
	σ_{ep}	σ_{sp}	σ_{ap}
Mean	1.01	0.50	0.50
StDev	1.84	0.81	1.90

slightly during increasing RH scans, particularly at the beginning of an RH scan when $dRH/dtime$ is large. During a high RH “soak” where RH is held at $\sim 90\%$ for 20 min, the agreement is within the 2%–3% RH uncertainty (Figure 2). In this case, accounting for a slight cooling across the CAPS from 26.4 ± 0.2 °C to 26.0 ± 0.2 °C occurring from inlet to outlet of the CAPS-PM_{SSA} reduces the ΔRH to 0.7%. The mean of the two sensors is taken as the effective cell RH as described earlier. A summary comparison of sensor agreement is given in Table 2 expressed as ΔRH across the CAPS cell. Though we sought to minimize temperature gradients in the instrument as described in the methods above, the highest RH is often upstream of the CAPS-PM_{SSA} instrument, closer to the humidifier. As a result, deliquescence is observed at an instrument cell RH below literature values as the slight warming in the CAPS-PM_{SSA} pushes the deliquesced aerosol back down the super-saturated branch of the hysteresis loop. We thus report here the hydrated aerosol properties for deliquescent aerosols like ammonium sulfate.

To constrain light absorption by water vapor itself, σ_{ep} , σ_{sp} , and σ_{ap} measurements are shown for filtered air (Gelman Sciences, Inc. HEPA or similar) at $RH < 20\%$ and $RH = 80\%$ in Table 3. The difference at low- and high RH is negligible for light scattering, but a measurable difference is observed for light absorption and hence extinction. The high RH enhancement in absorption signal is $\sim 1 \text{ Mm}^{-1}$ (Table 3), attributable to water vapor absorption. The absorption

measurements at low- and high RH are statistically different while the scattering measurements are not (at the 99+% confidence level using a two-tail Student *t* test).

Using polystyrene latex spheres (PSLs, Duke Scientific, Inc., Fremont, CA, USA, refractive index $1.59 + 0i$), system particle loss tests were conducted. Internal optical calibration of the CAPS-PM_{SSA} involves setting σ_{sp} to match σ_{ep} using a non-absorbing aerosol with a $D_p = 100$ nm. We followed the approach of Onasch et al. (2015) regarding calibration; the effects of changing refractive index as a function of size are further discussed there and in the work by Modini et al. (2020). Calibrations were performed approximately daily before the experiments or as needed to minimize drift, and an instrument zero-air baseline was taken before each size was tested. After sonication to eliminate clumping, the PSLs were generated in solution in a nebulizer and size selected with a DMA (TSI, Inc., Shoreview, MN, USA, Model 3080) to eliminate the effects of PSL solution residue and agglomerates. Using the Mie light scattering model “MieAmigo” that was designed by the manufacturer for the CAPS instrument, the truncation errors were corrected. A custom PyMieScatt code was also developed to independently evaluate the truncation corrections. For 200, 500, and 1000 nm PSLs these corrections were approximately 0.3%, 6.7%, and 11.1%, respectively for the custom code versus 0.8%, 6.3%, and 13.6%, respectively for MieAmigo (Onasch et al. 2015), the differences within the 4% truncation uncertainty found in the work by Modini et al. (2020).

Particle loss was constrained by comparing the wet to dry ratio of light extinction and light scattering for PSLs (deviations below 1 suggest particle loss). This comparison examined approximately 2–5 min of data ($N \geq 30$ 5-s data) just before and after a valve switch from dry to humid lines while allowing a short time (~ 15 – 30 s) for stabilization. With PSLs, a ratio of ~ 1.0 is expected due to PSL negligible water uptake (Tan et al. 2013; Ye et al. 2009) (Figure 3a). The ratio of high (RH = 80%) to low (RH = 20%) light extinction coefficient (mean and standard deviation) was 1.00 ± 0.03 (range 0.95–1.04 for $n = 8$ sizes); the ratio for light scattering was 1.02 ± 0.03 (range 0.97–1.08). Overall, for $100 < D_p < 1000$ nm, the high- to low RH scattering and extinction ratios were measured within ± 0.03 of the expected 1.0 value for PSLs, constraining particle losses in the range of most interest. The size extremes show larger variability and discrepancies, particularly at 50 nm (Figure 3). We include the $D_p = 50$ nm datapoint to demonstrate acceptable diffusion

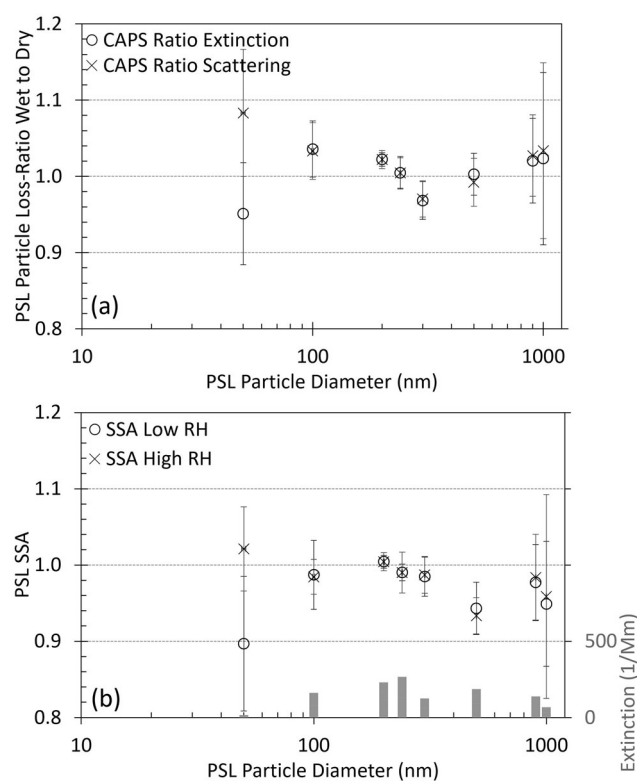


Figure 3. (a) PSL truncation-corrected measured particle loss as a function of diameter ($n = 8$ from $50 \text{ nm} < D_p < 1000 \text{ nm}$). Agreement is expressed as ratios of wet to dry extinction and scattering coefficients (with PSL ratio expected as 1.0 due to negligible water uptake). (b) PSL truncation-corrected single scattering albedo (SSA) as a function of PSL D_p . Means and standard deviations of ratios of data averaged over ~ 5 min ($n \geq 30$) and then ratioed during stable aerosol generation periods. The magnitude of the extinction coefficient for each size is shown as gray bars along the bottom axis where small signals at the extremes of D_p contributed to high variability.

losses. We stress that for this small size the scattering signal was quite low ($< 8 \text{ Mm}^{-1}$), even with the high number concentration generated by aerosolizing the entire sample size of 15 mL bottle of 50 nm PSLs in 200 mL solution needed in the atomizer.

Over the measured PSL sizes, truncation-corrected SSA (expected 1.0 due to negligible PSL absorption) was 0.97 ± 0.04 (range 0.9–1.01 for $n = 8$ sizes) at low RH and was 0.98 ± 0.03 (range 0.93–1.02) at high RH (Figure 3b). While the extinction measurement represents the total angular phase function, the scattering truncation error increases with the particle size due to increasing forward scattering. This results in SSA falling below one for the larger sizes $D_p > 500$ nm indicating that more careful truncation analysis will be needed for larger particles. Also, higher signal variability increases uncertainties for larger PSL particles as shown by error bars in Figure 3. Overall, for $100 < D_p < 300$ nm, SSA is measured within 0.03 of

the expected 1.0 value for PSLs. Higher variability and truncation errors explain the discrepancies at larger particle sizes ($D_p > 500$ nm). Comparing SSA at low- and high RH gives similar values for both extinction and scattering as shown in Figure 3b as expected for a hydrophobic PSL, excluding $D_p = 50$ nm case where signals were low.

3. Truncation correction algorithms: Mie amigo and PyMieScatt

Truncation quantifies the unmeasured light scattering due to the angular limits of the instrument, a consequence of the finite length of the instrument (Anderson et al. 1996; Anderson and Ogren 1998). Two approaches were taken to estimate truncation corrections: using the MieAmigo code developed for the CAPS-PM_{SSA} instrument and our customized PyMieScatt Algorithm (Sumlin, Heinson and Chakrabarty 2018). Both use the Lorentz-Mie scattering algorithms of Bohren and Huffman (1998). MieAmigo was developed by Aerodyne, Inc., Billerica, MA, USA, for use with the CAPS-PM_{SSA} and is written in C (Onasch et al. 2015). The use of the additional internal code for truncation corrections is to further develop this area of inquiry in follow-on studies, particularly for larger particles.

The second approach is our custom Python module that implements PyMieScatt, an open-source software developed for direct and inverse Mie calculations (Sumlin, Heinson, and Chakrabarty 2018). In determining the phase function, particles are assumed to be homogeneous spherical particles in the Mie scattering regime. The scattering efficiency for ideal and truncated conditions is calculated for evenly spaced locations along the central axis of the cavity of the CAPS-PM_{SSA}. The ideal phase function is integrated over the entire phase function $[0, 2\pi]$. The angles of integration for the truncated phase function are defined by trigonometric relations involving the position along the central axis and the diameter of the glass tube within the CAPS-PM_{SSA}, the diameter of the integrating sphere, and the distance between each position along the central axis with respect to both apertures. Since light can scatter into the integrating sphere from aerosol outside the integrating sphere, we extend the range along the central axis by 0.6 cm beyond the integrating sphere on either side with angles determined similarly. The ideal scattering efficiency is null for every position outside the integrating sphere. The truncation is then determined by integrating trapezoidally the ideal and truncated scattering efficiencies, Q , along the central axis of the cavity and taking a ratio of the two quantities ($\int Q_{\text{trunc}} / \int Q_{\text{ideal}}$). The truncation

correction is the inverse of this ratio, and the correction must be normalized to the truncation of the calibration aerosol to reduce uncertainties from the extinction's geometric correction. For generated mono- and poly dispersions, the agreement between MieAmigo and our custom code is strong ($< 1\%$), though larger discrepancies (3%–4%) arise for larger sizes and assumed log-normal distributions. Modini et al. (2020) devised an approach to merge the Fresnel equations with Mie calculations for improved accuracy for calculating the truncation in CAPS-PM_{SSA} monitors by explicitly accounting for light scattered off the inner surface of the glass tube inside the integrating sphere. Further exploration of the truncation loss and correction models is underway for larger sizes, but for purposes here (mostly small diameter monodispersions) we consider the reflection modification to the truncation correction to be within the measurement uncertainty. Where the PyMieScatt algorithm used is noted in the text. As discussed later, the truncation corrections were evaluated using ammonium sulfate size resolved $f(\text{RH})$ measurements (Section 4.2) and the empirical calibration scheme tested on size selected dry nigrosin using photoacoustic observations (Section 4.3).

4. Laboratory experiments

4.1. Laboratory measurements of $f(\text{RH})$ for light scattering and absorbing species

Our approach was to measure well-characterized pure systems with varied and known optical properties and evaluate our two distinct truncation schemes and develop calibration protocols. We tested the H-CAPS-PM_{SSA} with three laboratory-generated aerosols including light scatterers (ammonium sulfate, levoglucosan) and light absorbers (nigrosin). Ammonium sulfate and nigrosin are standard laboratory species used for calibration of aerosol light scattering and absorption instruments, respectively. We also performed independent measurements on dry size selected nigrosin particles with a photoacoustic spectrometer and our CAPS to demonstrate consistency. Mixtures of light scattering and absorbing species and ambient aerosol studies have also been measured, and manuscripts are in preparation.

Unless otherwise described, aerosols were generated in the Center for Aerosol Forensics (CAFÉ) laboratory at Los Alamos National Laboratory using an aerosol nebulizer (TSI, Inc., Shoreview, MN, USA, Model 3079A or similar), a diffusion drier (Droplet Measurement Technologies, Inc., Boulder, CO, USA, Model ASSY 1110 or similar), and size selection using a scanning mobility particle sizing system (TSI, Inc.,

Shoreview, MN, USA, Model 3938 using the 3080L long column and 3750 CPC) using an X-ray source for charge neutralization (TSI, Inc. Model 3088). More details are given in previous manuscripts (Gomez et al. 2018; Romonosky et al. 2019). The output of the atomizer was relatively constant; however, to adjust for minor fluctuations in aerosol generation, the magnitude of scattering, extinction, and absorption are normalized to total particle concentration measured with a condensation nuclei counter (TSI, Inc. Model 3010 or similar) or an independent nephelometer (Ecotech, Inc., Warren, RI, USA, Aurora 450 nm) during an RH scan to normalize out dry signal variability.

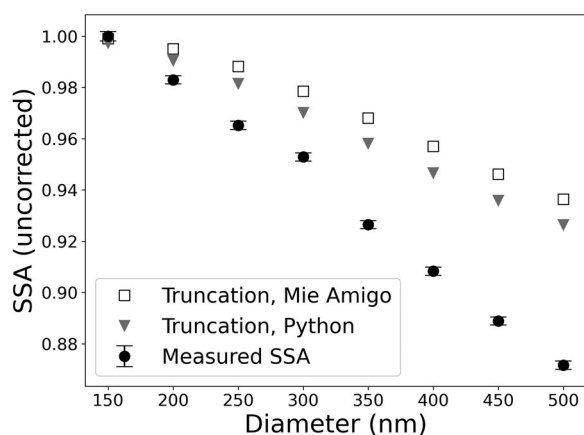


Figure 4. Truncation error effects for CAPS light scattering illustrated by the decrease in uncorrected measured single scattering albedo (SSA) with electrical mobility D_p for a purely scattering ammonium sulfate aerosol.

4.2. Size selected monodisperse ammonium sulfate

Previously we examined system particle loss with PSLs, finding reasonable particle loss. Notably, though with some variability due to PSL concentrations, a decrease in SSA below the expected value of 1.0 for PSLs for larger D_p (Figure 3) was due at least in part to angular truncation losses and imperfect corrections. Next, we explicitly measured and calculated using the two Mie codes, the SSA for size selected ammonium sulfate to compare truncation corrections schemes versus empirical measurements to better constrain this issue. A comparison of measured and Mie-calculated angular truncation for ammonium sulfate $[(\text{NH}_4)_2\text{SO}_4]$, Sigma Aldrich, Inc., St. Louis, MO, USA, MW 132.14 g/mol, CAS 7783-20-2] from the CAPS- PM_{SSA} is shown in Figure 4 as a function of electrical mobility diameter (D_p). This is expressed as the SSA as a function of D_p which should be 1.0 for ammonium sulfate and independent of D_p . As D_p increased from 150 nm, uncorrected measured SSA drops below 0.9 at $D_p = 500$ nm (Figure 4). Estimated truncation error accounts for much but not all this. The residual error that grows at larger sizes can result from imperfect truncation correction, multiply charged particle effects, and/or other sources of uncertainty that we will continue to investigate. For reference, the truncation errors calculated in the MieAmigo code grew from <1 to 7% increasing with particle size. Our PyMieScatt algorithm gave larger truncation corrections than Mie Amigo, though both underpredicted it for large D_p . Using radiative transfer calculations, Liu

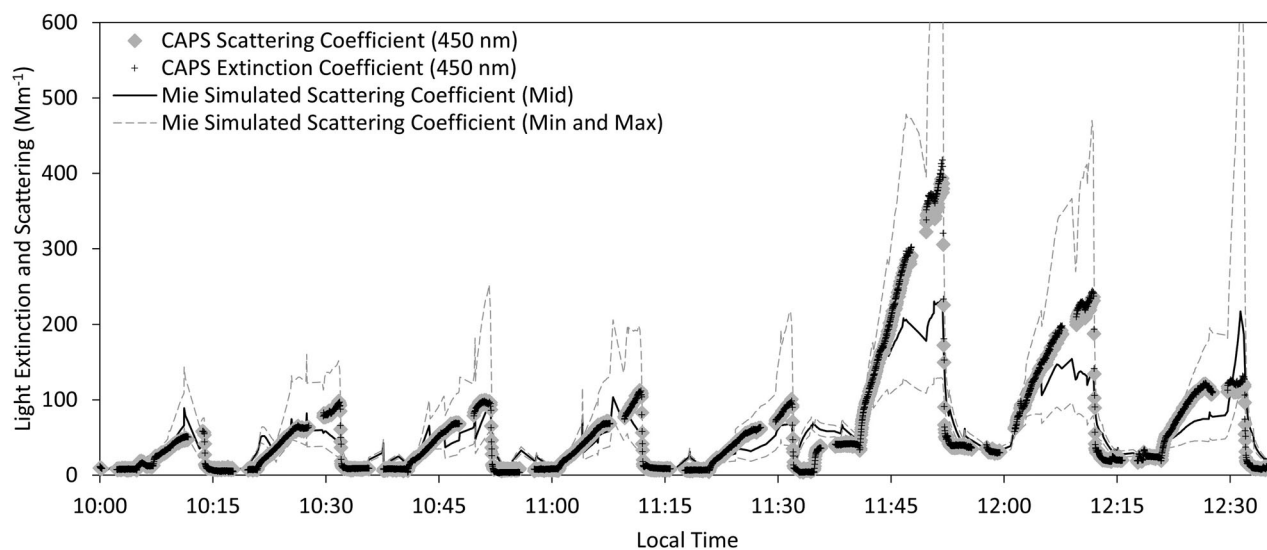


Figure 5. Repeated measurements of light extinction and scattering with deliquesced ammonium sulfate during eight increasing RH scans ($\sim 20\% < \text{RH} < 85\%$) in comparison with simulated Mie calculations. The min and max represent calculations with the uncertainties in input parameters (size, concentration, refractive index, diameter growth factors, and RH).

et al. (2018) showed that the reflectivity of the glass tube surrounding the cavity can enhance the truncation, especially for larger aerosol with greater forward scattering. This is not accounted for in either correction algorithm and is an area that needs refinement. For our further study, we choose to use the empirical ammonium sulfate SSA curve to calibrate our effective size-dependent correction that includes truncation, speckling, and other effects, and we evaluate it further with dry nigrosin.

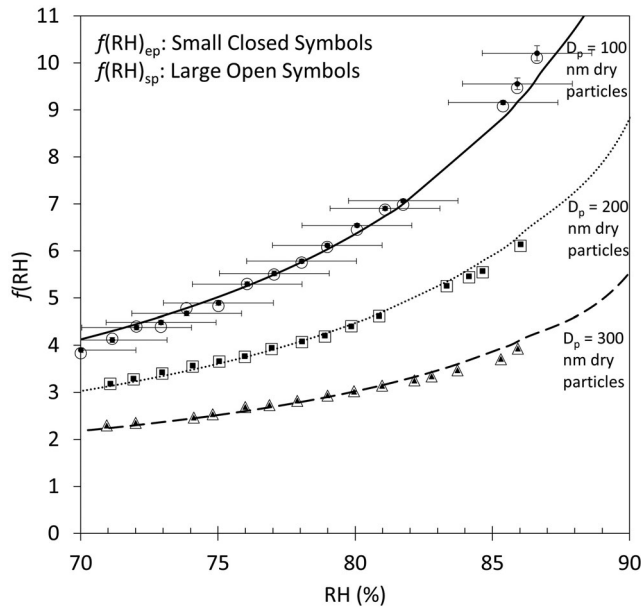


Figure 6. Comparison of $f(\text{RH})$ for light scattering and extinction for pure ammonium sulfate (dry conditions $\text{RH} < 40\%$).

Table 4. Best fit values for optical κ_{ep} and κ_{sp} (averaged for $\text{RH} > 70\%$) for pure ammonium sulfate as a function of dry ($\text{RH} < 40\%$) size (absorption is negligible).

D_p (nm)		κ_{ep}	κ_{sp}
100	Mean	1.34	1.33
	StDev	0.05	0.05
200	Mean	0.87	0.86
	StDev	0.02	0.02
300	Mean	0.50	0.51
	StDev	0.02	0.02

Table 5. Comparison of values of $f(\text{RH})_{\text{ep}}$ for ammonium sulfate.

Ammonium sulfate study	Technique	Dry ($\text{RH} < 40\%$) size	$f(\text{RH} = 80)_{\text{ep}}$
Zhou et al. (2020)	Broadband Cavity Enhanced Aerosol Extinction Spectrometry 532 nm	200 nm	3.17 ± 0.05
		300 nm	2.83 ± 0.10
Brem et al. (2012)	CRDS Nephelometer 467 nm	$D_p < 500$ nm polydisperse	~ 3.7
Garland et al. (2007)	CRDS (σ_{ep} only) 532 nm		200
Michel Flores et al. (2012)	CRDS (σ_{ep} only) 532 nm	300	3.0 ± 0.4
		200	3.6 ± 0.43
		300	3.13 ± 0.44
This study	Cavity Attenuated Phase Shift 450 nm	100	6.43 ± 0.52
		200	4.40 ± 0.21
		300	3.08 ± 0.20

Absorption is negligible and thus $f(\text{RH})_{\text{sp}}$ is equivalent to $f(\text{RH})_{\text{ep}}$.

A time series of truncation-corrected measured light scattering cycling through several RH scans versus Mie calculations is given in Figure 5 for ammonium sulfate. Ammonium sulfate is a negligible absorber with dry complex refractive index parameterized as a function of RH and λ in the study by Cotterell et al. (2017). The minimum to maximum envelope indicated is the range of Mie-simulated values considering the following uncertainties: $\pm 2\%$ for refractive index (~ 0.03), $\pm 10\%$ for measured particle concentration, and $\pm 4\%$ for RH. The latter uncertainty is an upper estimate based upon the sum of manufacturer uncertainty at high RH (3%) and the typical gradient observed through the optical cell as described earlier (1%).

Measurements of $f(\text{RH})$ for size selected pure ammonium sulfate, $(\text{NH}_4)_2\text{SO}_4$, are shown in Figure 6. Light scattering and extinction follow nearly identical $f(\text{RH})$ curves (negligible absorption) (Figure 6). During the RH scan, the independent light extinction and scattering measurements were strongly correlated with $R^2 > 0.999$ throughout the RH range. Brock, Wagner, Anderson, Attwood et al. (2016) provided a framework to quantify the hygroscopicity in optical terms using the volume-weighted κ_{ep} model, analogous to single-parameter κ -Köhler theory (Petters and Kreidenweis 2007). The retrieved best-fit hygroscopicity for pure ammonium sulfate is $\kappa_{\text{ep}} = 0.50 \pm 0.02$ for $D_p = 300$ nm (Table 4). A summary of hygroscopicity measured here for ammonium sulfate compares well to literature values as summarized in Table 5.

4.3. Size selected nigrosin

H-CAPS-PM_{SSA} measurements of dry size-selected monodisperse nigrosin ($\text{C}_{22}\text{H}_{14}\text{N}_6\text{Na}_2\text{O}_9\text{S}_2$, Alfa-Aesar, Inc., MW 616.5 g/mol, CAS Number 8005-03-6) were compared with a $3\text{-}\lambda$ photoacoustic spectrometer (PASS-3 at 405, 532, and 781 nm) (Flowers et al. 2010). The independent PASS-3 allows assessment for a dry absorbing aerosol of the size-dependent

truncation error correction matching the ammonium sulfate SSA of 1 from Figure 4, plus other systematic biases such as speckling (Liu et al 2018). The PASS-3 has much larger uncertainty and lower sensitivity than the CAPS-PM_{SSA} but no truncation errors, so it allows testing this approach. The PASS-3 is adjusted to 450 nm with σ_{ap} at 405 nm and Absorption Ångström Exponent (AAE) at the appropriate wavelength pair. We also stress that the absorption features of nigrosin in the blue are poorly characterized and introduce additional uncertainty. This is only possible at dry conditions (RH < 40%) with the PASS-3.

Despite uncertainties due to a nigrosin absorption

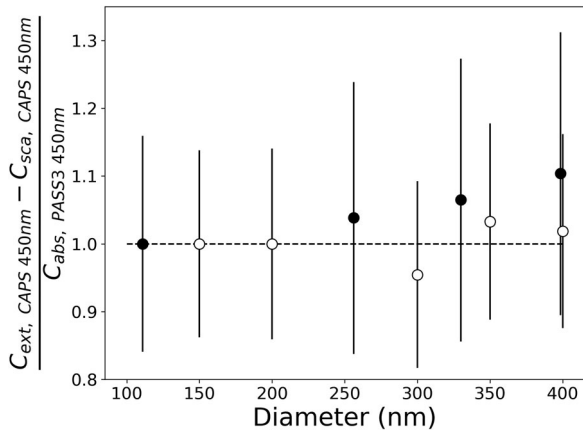


Figure 7. For dry nigrosin (RH < 40%), the ratio of measured and empirically corrected light absorption for two instruments (CAPS-PM_{SSA}/PASS-3 that uses the ammonium sulfate SSA = 1 calibration via Figure 4). The PASS-3 σ_{ap} at 450 nm was calculated from 405 nm PASS-3 σ_{ap} and AAE values. The open circles and closed circles show observations made over six months apart after a few updates by different operators to demonstrate stability.

peak in this spectral region, the instruments show consistency for dry conditions. In Figure 7, we show the truncation-corrected CAPS-PM_{SSA} and PASS-3 absorption cross-section ratios. The open and filled circles represent experiments performed over six months apart establishing the long-term instrument stability. Although the uncertainties in the measured ratios are significant, Figure 7 clearly shows that the size-dependent truncation-corrected dry σ_{ap} from the CAPS-PM_{SSA} agrees within experimental uncertainties with the PASS-3. For $D_p < 250$ nm for dry nigrosin, where truncation error is very small, the ratio is ~ 1.0 . For intermediate sizes $250 < D_p < 350$ nm, the ratio is 1 ± 0.05 , and increases to ~ 1.1 at $D_p = 400$ nm. Above 400 nm, the corrections and the uncertainty become large, and the CAPS-PM_{SSA} systematic bias is significant. Therefore, we recommend limiting the RH dependent measurements for SSA and absorption $f(\text{RH})$ studies to $D_p < 400$ nm as more work is needed for larger particles.

We also performed $f(\text{RH})$ measurements on small nigrosin particles, and Figure 8 shows twelve repeating RH scans from dry to RH $\sim 85\%$. The PASS-3 measured σ_{ap} in parallel (also shown) gave bracketing absorption values providing independent confirmation with average dry absorption during the experiment of 59 Mm^{-1} (PASS, 405 nm) < 68 Mm^{-1} (CAPS, 450 nm) < 79 Mm^{-1} (PASS, 532 nm). CAPS σ_{ep} and σ_{sp} show consistent responses compared to the model simulations in the top two panels in Figure 8. Uncertainties in RH, particle concentration, and refractive index are propagated into the calculation to give the minimum–maximum envelope as shown in

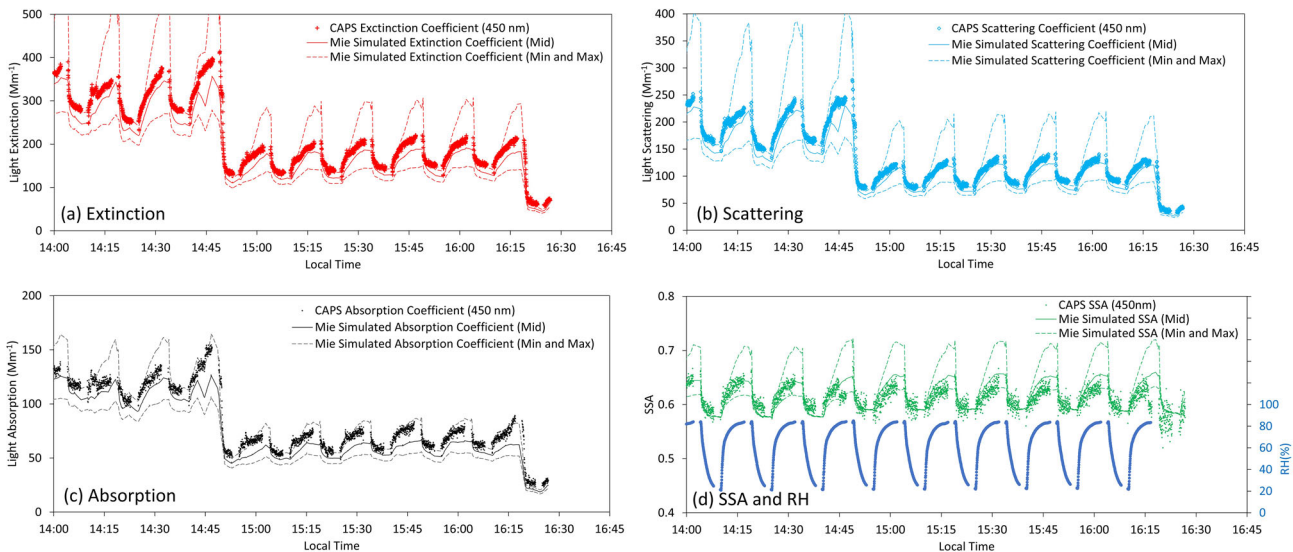


Figure 8. Nigrosin (a) σ_{ep} , (b) σ_{sp} , (c) σ_{ap} including data from a multi- λ PASS for comparison, and (d) single scattering albedo (SSA) and RH (right y-axis) time series measured with the H-CAPS-PM_{SSA} for twelve RH scans, compared with Mie simulations.

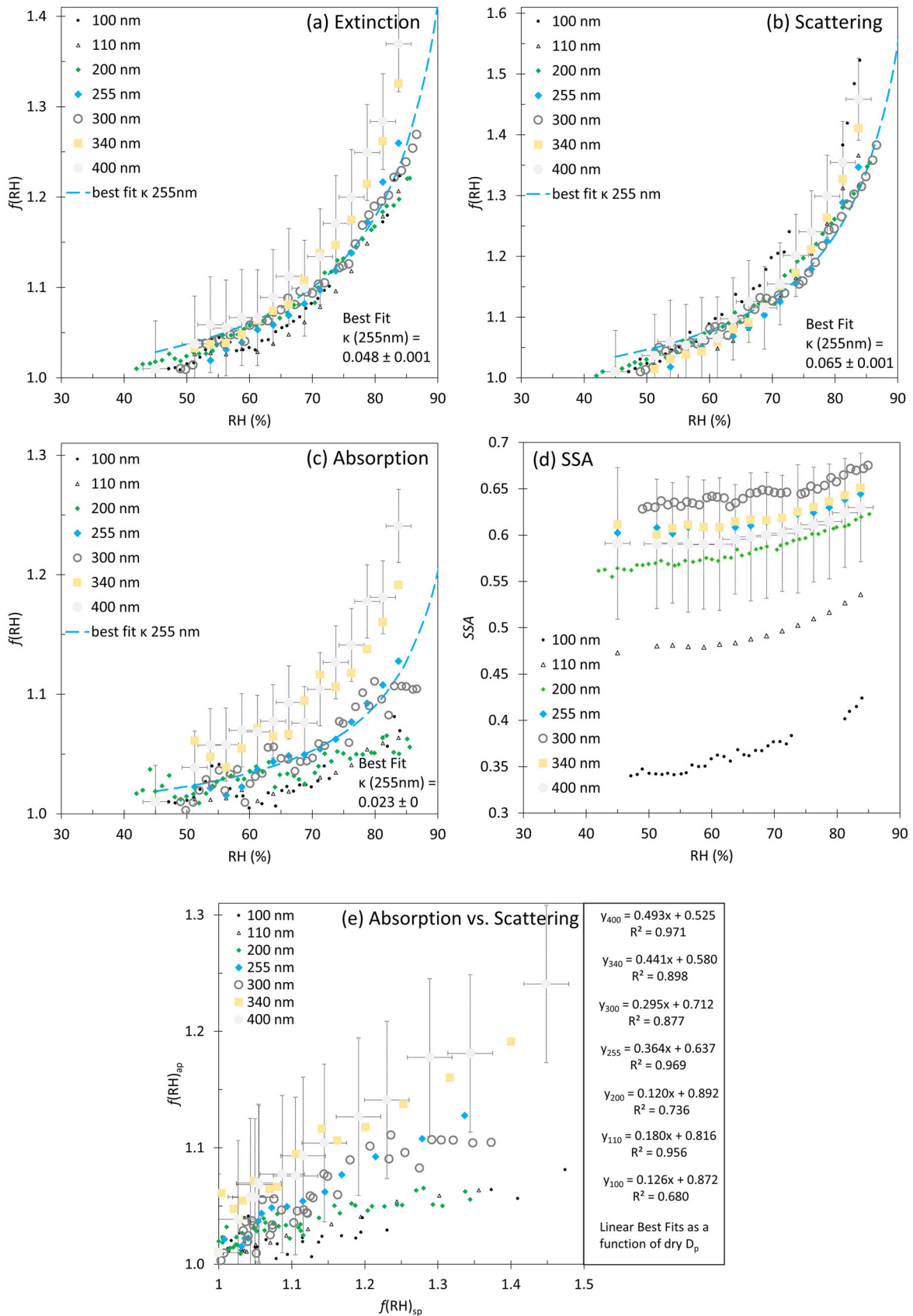


Figure 9. Comparison of $f(\text{RH})$ (where “dry” $\text{RH} < 40\%$) for pure nigrosin measured with H-CAPS-PM_{SSA} and corrected for truncation, for (a) σ_{ep} , (b) σ_{sp} , (c) σ_{ap} , (d) SSA(RH), and (e) $f(\text{RH})_{\text{ap}}$ versus $f(\text{RH})_{\text{sp}}$. Representative best fit optical κ -lines are shown for dry $D_p = 255$ nm. Representative error bars show the standard deviation of the given $f(\text{RH})$ parameter and $\pm 2\%$ RH sensor accuracy.

Figure 8, and measurements generally are within that expected range.

For size-selected nigrosin, $f(\text{RH})_{\text{ep}}$, σ_{sp} , κ_{ap} are given as separate panels (Figures 9a–c, respectively) for the selected dry sizes. With larger sizes for nigrosin, the uncertainties in σ_{ap} and $f(\text{RH})_{\text{ap}}$ increase. It is also evident in the SSA trends with size as discussed later. The nigrosin $f(\text{RH})_{\text{sp}}$ curves exceed $f(\text{RH})_{\text{ep}}$ resulting in a small though measurable $f(\text{RH})_{\text{ap}}$ that monotonically increases with RH. Generally, $f(\text{RH})_{\text{ap}}$ for nigrosin increases with dry size ranging from ~ 1.05 to 1.2 at $\text{RH} = 80\%$ (Figure 9c). For $D_p = 100$ and 300 nm sizes, the values for absorption enhancement ($f(\text{RH})_{\text{ap}} = 80\%$) are slightly lower than the values of 1.12 – 1.18 reported by Zhou et al. (2020). Representative error bars shown in Figure 9 indicate the variability for the given parameter ($\sim 5\%$) for $\text{RH} < 40\%$ which is considered “dry” here. We estimate experimental uncertainties of approximately ± 0.03 for $f(\text{RH})_{\text{ap}}$ using the standard deviation of dry $f(\text{RH})$.

Figure 9d shows the aerosol SSA for nigrosin for dry sizes: $D_p = 100, 110, 200, 255, 300, 340,$ and 400 nm. The smallest particles with dry $D_p = 100$ nm are the most strongly absorbing whereas larger particles show higher SSA as predicted by Mie Theory. SSA(RH) increases by ~ 0.1 from low to high RH and

Table 6. Best fit values κ ($\text{RH} > 80\%$) for optical parameters for pure nigrosin as a function of dry size.

D_p (nm)		κ_{ep}	κ_{sp}	κ_{ap}
100	Mean	0.029	0.074	0.006
	StDev	0.008	0.015	0.006
110	Mean	0.039	0.069	0.011
	StDev	0.001	0.000	0.001
200	Mean	0.039	0.061	0.011
	StDev	0.003	0.004	0.002
255	Mean	0.048	0.065	0.023
	StDev	0.001	0.001	0.000
300	Mean	0.041	0.056	0.020
	StDev	0.003	0.004	0.004
340	Mean	0.060	0.075	0.035
	StDev	0.002	0.003	0.000
400	Mean	0.066	0.083	0.042
	StDev	0.005	0.005	0.004

Since κ_{ep} is a composite rather than a sum of κ_{sp} and κ_{ap} , it is intermediate such that $\kappa_{\text{sp}} > \kappa_{\text{ep}} > \kappa_{\text{ap}}$.

Table 7. Comparison of values of $f(\text{RH})$ for light absorption for nigrosin.

Nigrosin study	Technique	Dry size	$f(\text{RH} = 80)$ extinction	$f(\text{RH} = 80)$ scattering	$f(\text{RH} = 80)$ absorption
Zhou et al. (2020)	Cavity Enhanced Aerosol Extinction Spectrometry 532 nm	200 nm	1.22 ± 0.00	1.34 ± 0.00	1.12 ± 0.01
		300 nm	1.26 ± 0.01	1.34 ± 0.02	1.18 ± 0.01
Brem et al. (2012)	CRDS & Nephelometer 467 nm	$D_p < 500$ nm polydisperse	~ 1.26	~ 1.33	~ 1.2
Michel Flores et al. (2012)	CRDS (σ_{ep} only) 532 nm	200	1.18 ± 0.06	NA	NA
		300	1.19 ± 0.04		
This study	Cavity Attenuated Phase Shift 450 nm	110	1.15 ± 0.02	1.27 ± 0.04	1.05 ± 0
		255	1.18 ± 0.03	1.25 ± 0.05	1.09 ± 0.01
		340	1.23 ± 0.03	1.28 ± 0.04	1.14 ± 0.02

Dry conditions are defined similarly in the studies as $\text{RH} < 40\%$. Uncertainties shown are estimated as described in the text and shown in Figure 9.

is sensitive to D_p . Using volume mixing rules and a dry refractive index for nigrosin of $1.635 + 0.175i$, intermediate to the $1.63 + 0.13i$ found at 450 nm (Liu et al. 2013) and $1.63 + 0.20i$ found at 420 nm (Washenfelder et al. 2013), we can calculate SSA. SSA is 0.3 for $D_p = 100$ nm and asymptotes to 0.7 for $D_p > 255$ nm, which is consistent with measured trends for smaller D_p in Figure 9d. We see in Figure 9d that the SSA increases with D_p at a given humidity until 300 nm and then drops for $D_p > 300$ nm. The angular truncation correction and its calculational uncertainty increases with particle size requiring caution for measurements for $D_p > 400$ nm. The lower SSA range for the largest dry D_p , $0.55 < \text{SSA} < 0.65$, may be driven by a lower imaginary refractive index for nigrosin as found in other studies (Lack et al. 2006). Contributions from multiply charged particles for larger sizes that cannot be removed from the population are possible for larger sizes but still likely small.

Finally, Figure 9e shows the relationship between $f(\text{RH})$ for light scattering and light absorption for the particle dry sized measured with nigrosin (Cappa 2020). The relationship is generally linear, though varies with dry size where larger D_p show larger $f(\text{RH})_{\text{ap}}$ as indicated by the larger slopes in Figure 9e. The linear fits can be used to parameterize the less-commonly measured $f(\text{RH})_{\text{ap}}$ using $f(\text{RH})_{\text{sp}}$ with knowledge of the aerosol composition and size. The retrieved best fit κ -values (for $\text{RH} > 80\%$) for nigrosin are given in Table 6. All sizes show increases in absorption with RH that can be fit with $0.004 < \kappa_{\text{ap}} < 0.08$ (Table 6). A summary of nigrosin absorption $f(\text{RH})$ values compared to literature sources is given in Table 7.

4.4. Polydisperse levoglucosan

Levoglucosan ($\text{C}_6\text{H}_{10}\text{O}_5$ or 1,6-anhydro- β -D-glucopyranose, Sigma-Aldrich, Inc., St. Louis, MO, USA, MW = 162.14 g/mol, CAS Number 498-07-7) is a biomass smoke marker produced by incomplete combustion of

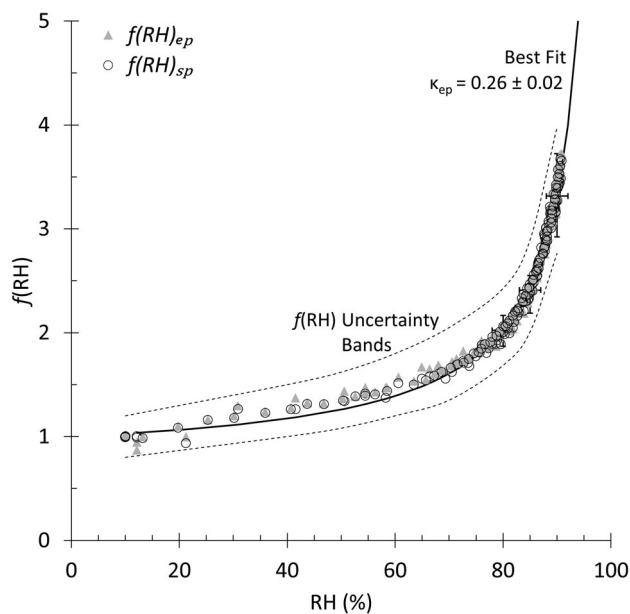


Figure 10. Hygroscopic growth curves $f(\text{RH})_{\text{ep}}$ and $f(\text{RH})_{\text{sp}}$ for polydispersed pure levoglucosan aerosol generated in the laboratory. σ_{ap} is negligible for this species. Means and standard deviations over $\pm 2\%$ RH bins are shown at RH = 80%, 85%, and 90%. Dry condition is RH < 40%, and best-fit κ_{ep} curve is shown.

lignin (Engling et al. 2006; Sullivan et al. 2008). Levoglucosan comprises up to 10%–30% of organic carbon in smoke (Aiken et al. 2009; Ward et al. 2006). It is abundant in smoke particles with $D_p < 0.5 \mu\text{m}$ (Engling et al. 2009). Its lifetime was measured as 0.7–2.2 days, primarily limited by OH radical oxidation (Hennigan et al. 2010).

Past studies demonstrate that levoglucosan is hydrophilic, showing continuous water uptake with no observable deliquescence or hysteresis and a diameter growth factor of 1.18 and 1.38 at 80% and 90% RH, respectively for 100 nm dry particles (Mochida and Kawamura 2004). Likewise, diameter growth factors D/D_0 (RH = 80%) of 1.21 and D/D_0 (RH = 90%) ~ 1.39 were measured for levoglucosan with $D_p = 100$ nm dry particles (Jing et al. 2017). Mixed inorganic levoglucosan smoke deliquescence RH (DRH) fell by 0–8% with increasing organic fraction disappearing completely at high-organic fractions (Parsons, Knopf and Bertram 2004). In mixtures with KCl, it lowered the DRH from 84% to <80% and reduced the hygroscopicity as compared with pure KCl. Though levoglucosan has been associated with absorptive properties of biomass burning aerosols in several studies (Lee et al. 2020; Teich et al. 2017), its imaginary refractive index has been measured to be zero (non-absorbing) at 550 nm using high-performance

liquid chromatography photodiode array spectroscopy (Schkolnik et al. 2007).

Controlled-RH measurements of polydispersed aerosol generated as discussed in Section 4.1 using levoglucosan are shown for light scattering and extinction in Figure 10. The small quantity of material available to us allowed two RH-scan experiments with a small diameter polydispersed aerosol (geometric mean $D_{p,g} = 56$ nm, $\sigma_g = 1.84$). Truncation corrections at such a small size are small, ~ 1.01 for dry and 1.02 at RH = 80%. To normalize out minor fluctuations in aerosol generation, the dry light scattering coefficient from a dry nephelometer (Ecotech Aurora 450 nm) in parallel was used in real-time (<10% changes in dry signal). The light absorption component from levoglucosan was negligible as measured here, and hence light scattering and extinction were equivalent in both magnitude and hygroscopic response during two RH scans (Figure 10). Our measurements demonstrate that levoglucosan is moderately hydrophilic with κ_{ep} and $\kappa_{\text{sp}} = 0.26 \pm 0.01$, and $f(\text{RH} = 80\%) = 2.02 \pm 0.08$ for a dry size distribution with $D_{p,g} = 56$ nm, $\sigma_g = 1.84$. This single-component organic compound found in smoke is more hydrophilic than typically measured organic carbon-dominated (Quinn et al. 2005) or aged ambient smoke aerosols (Carrico et al. 2005). Garland et al. (2007) found a range of $1.5 < f(\text{RH} = 80) < 1.7$ for levoglucosan, for a larger dry size ($D_{p,g} = 250$ nm) though. Consistently, a moderately hydrophilic response was observed for pure levoglucosan with Hygroscopic Tandem Differential Mobility Analyzer (HTDMA) measurements by Jing et al. (2017) with diameter growth factor of 1.28 at RH = 85% and 1.39 at RH = 90% for $D_p = 100$ nm dry particles. Part of the uncertainty for levoglucosan is that it exhibits no clear deliquescence point and likely binds water down to low RH adding uncertainty to the “baseline” dry conditions ($D/D_0 \sim 1$ –1.05 depending upon water retention at RH < 40%), impacting both dry size and refractive index (Koehler et al. 2006).

5. Summary and conclusion

Despite key advancements, RH-dependent optical property measurements continue to be challenging, particularly for absorbing aerosols. We report the construction, validation, and first measurements that confirm reliable performance of a new humidified cavity attenuated phase shift particulate matter single scattering albedo (H-CAPS-PM_{SSA}) instrument for measuring RH dependence of aerosol optical properties. It

allows controlled humidity measurements using the CAPS-PM_{SSA} (Aerodyne, Inc., Billerica, MA, USA) that combines light extinction using the cavity attenuated phase shift technique and light scattering using an integrating sphere nephelometer. Our new technique reliably quantifies the RH dependence of light absorption as well as aerosol SSA by using scattering and extinction measurements of the same aerosol volume. We show that it is a precise, accurate, and robust instrument that uses a commercially available instrument at its heart and can be replicated.

The H-CAPS-PM_{SSA} uses a controlled-RH system developed for controlling and measuring the hygroscopic response of absorbing aerosols and provides a direct measurement of SSA as a function of RH. The H-CAPS-PM_{SSA} uses a membrane-based flow-through humidifier with a PID controller to control the humidification process and is enclosed in a thermoelectrically air-conditioned enclosure for temperature uniformity. Several instrument modifications included increasing sample flow rate, removing the sample pump and other modifications to reduce sample heating, and locating RH/temperature sensors immediately upstream and downstream of the sample cell. The system was tested for particle loss, which was shown to be small, RH characterization, and light scattering angular truncation error corrections.

The system details are documented herein as well as the first results with ammonium sulfate, nigrosin, and levoglucosan. Measurements with light scattering and absorbing compounds were used to validate instrumental performance, and results were within experimental uncertainties for the pure scattering and absorbing aerosols. Careful analysis of computed scattering truncation corrections show that they are small and accurate for particles with diameters $D_p < 400$ nm. Proper truncation corrections that grow with size is critical and limits our current operation regime to $D < 400$ nm. Several instrument improvements are underway, including adding a second CAPS-PM_{SSA} instrument to run continuously as a “dry” reference state measurement. The instrument will be used to further diagnose the response of light-absorbing mixtures to the influence of RH.

Acknowledgment

Data are available by emailing the corresponding author (kip.carrico@nmt.edu).

Funding

This material is a part based upon work supported by the National Science Foundation under Grant No.1832813 (CMC, SG). This work was supported in part by the U.S. Department of Energy, Office of Science, Office of Workforce Development for Teachers and Scientists (WDTS) under the Visiting Faculty Program (VFP) (CMC, JTL), and the DOE Student Undergraduate Laboratory Intern Program (JTL, JK). TJC was partially supported by a fellowship through a DOE Office of Science Graduate Student Research Program. The New Mexico Consortium is gratefully acknowledged for financial support in this research (CMC, JTL, SG, JK, CD). The acquisition of the CAPS-PM_{SSA}, some assembly parts, laboratory evaluation, and testing were primarily done at LANL and supported primarily by the U.S. Department of Energy’s Atmospheric System Research, Office of Science, Office of Biological and Environmental Research’s Atmospheric System Research program under grant F265 (PI MKD) as well as LANL’s Laboratory Directed Research Exploratory Research (LDRD) project 20200035DR (PI MKD). Los Alamos National Laboratory is operated for the DOE by Los Alamos National Security under contract DE-AC52-06NA25396. We acknowledge LANL’s LDRD and the Center for Space and Earth Science and the support of Sanna Sevanto and Petr Chylek at LANL.

ORCID

Christian M. Carrico  <http://orcid.org/0000-0002-1949-3824>

Tyler J. Capek  <http://orcid.org/0000-0002-9831-4360>

Kyle J. Gorkowski  <http://orcid.org/0000-0002-3750-1189>

Sabina Gulick  <http://orcid.org/0000-0002-6263-3597>

James E. Lee  <http://orcid.org/0000-0002-9137-1530>

Charlotte Dungan  <http://orcid.org/0000-0002-0084-3935>

Allison C. Aiken  <http://orcid.org/0000-0001-5749-7626>

Timothy B. Onasch  <http://orcid.org/0000-0001-7796-7840>

Andrew Freedman  <http://orcid.org/0000-0002-5598-6626>

Claudio Mazzoleni  <http://orcid.org/0000-0002-2398-0721>

Manvendra K. Dubey  <http://orcid.org/0000-0002-3492-790X>

References

- Aiken, A. C., D. Salcedo, M. J. Cubison, J. A. Huffman, P. F. DeCarlo, I. M. Ulbrich, K. S. Docherty, D. Sueper, J. R. Kimmel, D. R. Worsnop, et al. 2009. Mexico city aerosol analysis during milagro using high resolution aerosol mass spectrometry at the urban supersite (t0) – Part 1: Fine particle composition and organic source apportionment. *Atmos. Chem. Phys.* 9 (17):6633–53. doi: 10.5194/acp-9-6633-2009.
- Anderson, T. L., D. S. Covert, S. F. Marshall, M. L. Laucks, R. J. Charlson, A. P. Waggoner, J. A. Ogren, R. Caldwell, R. L. Holm, F. R. Quant, et al. 1996. Performance characteristics of a high-sensitivity, three-wavelength, total scatter/backscatter nephelometer. *J. Atmos. Oceanic Technol.*

- 13 (5):967–86. > 2.0.co;2. doi:10.1175/1520-0426(1996)013 <0967:pcoahs.
- Anderson, T. L., and J. A. Ogren. 1998. Determining aerosol radiative properties using the tsi 3563 integrating nephelometer. *Aerosol Sci. Technol.* 29 (1):57–69. doi:10.1080/02786829808965551.
- Arnott, W., H. Moosmuller, P. Sheridan, J. Ogren, R. Raspert, W. Slaton, J. Hand, S. Kreidenweis, and J. Collett. 2003. Photoacoustic and filter-based ambient aerosol light absorption measurements: Instrument comparisons and the role of relative humidity. *J. Geophys. Res.* 108 (D1): AAC 15-1–AAC 15-11. doi:10.1029/2002JD002165.
- Arnott, W. P., H. Moosmuller, C. F. Rogers, T. F. Jin, and R. Bruch. 1999. Photoacoustic spectrometer for measuring light absorption by aerosol: Instrument description. *Atmos. Environ.* 33 (17):2845–52. doi:10.1016/S1352-2310(98)00361-6.
- Baynard, T., R. M. Garland, A. R. Ravishankara, M. A. Tolbert, and E. R. Lovejoy. 2006. Key factors influencing the relative humidity dependence of aerosol light scattering. *Geophys. Res. Lett.* 33 (6):L06813. doi:10.1029/2005GL024898.
- Baynard, T., E. R. Lovejoy, A. Pettersson, S. S. Brown, D. Lack, H. Osthoff, P. Massoli, S. Ciciora, W. P. Dube, and A. R. Ravishankara. 2007. Design and application of a pulsed cavity ring-down aerosol extinction spectrometer for field measurements. *Aerosol Sci. Technol.* 41 (4): 447–62. doi:10.1080/02786820701222801.
- Bohren, C. F., and D. R. Huffman. 1998. *Absorption and scattering of light by small particles*. Weinheim, Germany: Wiley-VCH Verlag GmbH & Co. KGaA.
- Bond, T. C., T. L. Anderson, and D. Campbell. 1999. Calibration and intercomparison of filter-based measurements of visible light absorption by aerosols. *Aerosol Sci. Technol.* 30 (6):582–600. doi:10.1080/027868299304435.
- Bond, T. C., and R. W. Bergstrom. 2006. Light absorption by carbonaceous particles: An investigative review. *Aerosol Sci. Technol.* 40 (1):27–67. doi:10.1080/02786820500421521.
- Bond, T. C., S. J. Doherty, D. W. Fahey, P. M. Forster, T. Berntsen, B. J. DeAngelo, M. G. Flanner, S. Ghan, B. Karcher, D. Koch, et al. 2013. Bounding the role of black carbon in the climate system: A scientific assessment. *J. Geophys. Res. Atmos.* 118 (11):5380–552. doi:10.1002/jgrd.50171.
- Brem, B., F. Gonzalez, S. Meyers, T. Bond, and M. Rood. 2012. Laboratory-measured optical properties of inorganic and organic aerosols at relative humidities up to 95. *Aerosol Sci. Technol.* 46 (2):178–90. doi:10.1080/02786826.2011.617794.
- Brock, C., N. Wagner, B. Anderson, A. Attwood, A. Beyersdorf, P. Campuzano-Jost, A. Carlton, D. Day, G. Diskin, T. Gordon, et al. 2016. Aerosol optical properties in the southeastern united states in summer – Part 1: Hygroscopic growth. *Atmos. Chem. Phys.* 16 (8): 4987–5007. doi:10.5194/acp-16-4987-2016.
- Brock, C., N. Wagner, B. Anderson, A. Beyersdorf, P. Campuzano-Jost, D. Day, G. Diskin, T. Gordon, J. Jimenez, D. Lack, et al. 2016. Aerosol optical properties in the southeastern united states in summer – Part 2: Sensitivity of aerosol optical depth to relative humidity and aerosol parameters. *Atmos. Chem. Phys.* 16 (8): 5009–19. doi:10.5194/acp-16-5009-2016.
- Cappa, C. 2020. *Understanding the influence of water uptake on absorption by aerosols*. American Geophysical Union, A243-01, AGU Fall Meeting, online, December 2020.
- Cappa, C., T. Onasch, P. Massoli, D. Worsnop, T. Bates, E. Cross, P. Davidovits, J. Hakala, K. Hayden, B. Jobson, et al. 2012. Radiative absorption enhancements due to the mixing state of atmospheric black carbon. *Science* 337 (6098):1078–81. doi:10.1126/science.1223447.
- Cappa, C. D., D. A. Lack, J. B. Burkholder, and A. R. Ravishankara. 2008. Bias in filter-based aerosol light absorption measurements due to organic aerosol loading: Evidence from laboratory measurements. *Aerosol Sci. Technol.* 42 (12):1022–32. doi:10.1080/02786820802389285.
- Carrico, C., S. Gomez, M. Dubey, and A. Aiken. 2018. Low hygroscopicity of ambient fresh carbonaceous aerosols from pyrotechnics smoke. *Atmos. Environ.* 178:101–8. doi:10.1016/j.atmosenv.2018.01.024.
- Carrico, C., S. Kreidenweis, W. Malm, D. Day, T. Lee, J. Carrillo, G. McMeeking, and J. Collett. 2005. Hygroscopic growth behavior of a carbon-dominated aerosol in Yosemite national park. *Atmos. Environ.* 39 (8):1393–404. doi:10.1016/j.atmosenv.2004.11.029.
- Carrico, C., P. Kus, M. Rood, P. Quinn, and T. Bates. 2003. Mixtures of pollution, dust, sea salt, and volcanic aerosol during ace-Asia: Radiative properties as a function of relative humidity. *J. Geophys. Res.* 108 (D23):8650. doi:10.1029/2003JD003405.
- China, S., C. Mazzoleni, K. Gorkowski, A. C. Aiken, and M. K. Dubey. 2013. Morphology and mixing state of individual freshly emitted wildfire carbonaceous particles. *Nat. Commun.* 4 (1):2122. doi:10.1038/ncomms3122.
- Coen, M. C., E. Weingartner, A. Apituley, D. Ceburnis, R. Fierz-Schmidhauser, H. Flentje, J. S. Henzing, S. G. Jennings, M. Moerman, A. Petzold, et al. 2010. Minimizing light absorption measurement artifacts of the aethalometer: Evaluation of five correction algorithms. *Atmos. Meas. Tech.* 3 (2):457–74. doi:10.5194/amt-3-457-2010.
- Cotterell, M. I., R. E. Willoughby, B. R. Bzdek, A. J. Orr-Ewing, and J. P. Reid. 2017. A complete parameterisation of the relative humidity and wavelength dependence of the refractive index of hygroscopic inorganic aerosol particles. *Atmos. Chem. Phys.* 17 (16):9837–51. doi:10.5194/acp-17-9837-2017.
- Cross, E., T. Onasch, A. Ahern, W. Wrobel, J. Slowik, J. Olfert, D. Lack, P. Massoli, C. Cappa, J. Schwarz, et al. 2010. Soot particle studies instrument inter-comparison project overview. *Aerosol Sci. Technol.* 44 (8):592–611. doi:10.1080/02786826.2010.482113.
- de Faria, J., U. Bundke, M. Berg, A. Freedman, T. Onasch, and A. Petzold. 2017. Airborne and laboratory studies of an iagos instrumentation package containing a modified caps particle extinction monitor. *Aerosol Sci. Technol.* 51 (11):1240–53. doi:10.1080/02786826.2017.1355547.
- DeMott, P. J., A. J. Prenni, X. Liu, S. M. Kreidenweis, M. D. Petters, C. H. Twohy, M. S. Richardson, T. Eidhammer, and D. C. Rogers. 2010. Predicting global atmospheric ice nuclei distributions and their impacts on climate. *Proc.*

- Natl. Acad. Sci. U.S.A.* 107 (25):11217–22. doi:10.1073/pnas.0910818107.
- Diveky, M., S. Roy, J. Cremer, G. David, and R. Signorell. 2019. Assessing relative humidity dependent photoacoustics to retrieve mass accommodation coefficients of single optically trapped aerosol particles. *Phys. Chem. Chem. Phys.* 21 (9):4721–31. doi:10.1039/c8cp06980h.
- Drinovec, L., G. Močnik, P. Zotter, A. S. H. Prévôt, C. Ruckstuhl, E. Coz, M. Rupakheti, J. Sciare, T. Müller, A. Wiedensohler, et al. 2015. The “dual-spot” aethalometer: An improved measurement of aerosol black carbon with real-time loading compensation. *Atmos. Meas. Tech.* 8 (5):1965–79. doi:10.5194/amt-8-1965-2015.
- Duplissy, J., P. DeCarlo, J. Dommen, M. Alfarra, A. Metzger, I. Barmapadimos, A. Prevot, E. Weingartner, T. Tritscher, M. Gysel, et al. 2011. Relating hygroscopicity and composition of organic aerosol particulate matter. *Atmos. Chem. Phys.* 11 (3):1155–65. doi:10.5194/acp-11-1155-2011.
- El-Sayed, M. M. H., D. Amenumey, and C. J. Hennigan. 2016. Drying-Induced Evaporation of Secondary Organic Aerosol during Summer, *Environ. Sci. Technol.*, 50(7), 3626–3633, doi: <https://doi.org/10.1021/acs.est.5b06002>.
- Engling, G., C. M. Carrico, S. M. Kreidenweis, J. L. Collett Jr, D. E. Day, W. C. Malm, E. Lincoln, W. Min Hao, Y. Iinuma, and H. Herrmann. 2006. Determination of levoglucosan in biomass combustion aerosol by high-performance anion-exchange chromatography with pulsed amperometric detection. *Atmos. Environ.* 40:299–S311. doi:10.1016/j.atmosenv.2005.12.069.
- Engling, G., J. Lee, Y. Tsai, S. Lung, C. Chou, and C. Chan. 2009. Size-resolved anhydrosugar composition in smoke aerosol from controlled field burning of rice straw. *Aerosol Sci. Technol.* 43 (7):662–72. doi:10.1080/02786820902825113.
- Flowers, B. A., M. K. Dubey, C. Mazzoleni, E. A. Stone, J. J. Schauer, S. W. Kim, and S. C. Yoon. 2010. Optical-chemical-microphysical relationships and closure studies for mixed carbonaceous aerosols observed at Jeju Island; 3-laser photoacoustic spectrometer, particle sizing, and filter analysis. *Atmos. Chem. Phys.* 10 (21):10387–98. doi:10.5194/acp-10-10387-2010.
- Forrister, H., J. Liu, E. Scheuer, J. Dibb, L. Ziemba, K. L. Thornhill, B. Anderson, G. Diskin, A. E. Perring, J. P. Schwarz, et al. 2015. Evolution of brown carbon in wildfire plumes. *Geophys. Res. Lett.* 42 (11):4623–30. doi:10.1002/2015GL063897.
- Freedman, A. 2014. *Caps pmssa monitor: User manual*. Vol. 23. Billerica, MA: Aerodyne, Inc.
- Garland, R., A. Ravishankara, E. Lovejoy, M. Tolbert, and T. Baynard. 2007. Parameterization for the relative humidity dependence of light extinction: Organic-ammonium sulfate aerosol. *J. Geophys. Res.* 112 (D19):D19303. doi:10.1029/2006JD008179.
- Gomez, S., C. Carrico, C. Allen, J. Lam, S. Dabli, A. Sullivan, A. Aiken, T. Rahn, D. Romonosky, P. Chylek, et al. 2018. Southwestern us biomass burning smoke hygroscopicity: The role of plant phenology, chemical composition, and combustion properties. *J. Geophys. Res. Atmos.* 123 (10):5416–32. doi:10.1029/2017JD028162.
- Gordon, T. D., A. J. Prenni, J. R. Renfro, E. McClure, B. Hicks, T. B. Onasch, A. Freedman, G. R. McMeeking, and P. Chen. 2018. Open-path, closed-path, and reconstructed aerosol extinction at a rural site. *J. Air Waste Manag. Assoc.* 68 (8):824–35. doi:10.1080/10962247.2018.1452801.
- Gorkowski, K., T. Preston, and A. Zuend. 2019. Relative-humidity-dependent organic aerosol thermodynamics via an efficient reduced-complexity model. *Atmos. Chem. Phys.* 19 (21):13383–407. doi:10.5194/acp-19-13383-2019.
- Han, T., W. Xu, J. Li, A. Freedman, J. Zhao, Q. Wang, C. Chen, Y. Zhang, Z. Wang, P. Fu, et al. 2017. Aerosol optical properties measurements by a caps single scattering albedo monitor: Comparisons between summer and winter in Beijing. *J. Geophys. Res. Atmos.* 122 (4):2513–26. doi:10.1002/2016JD025762.
- Heintzenberg, J., A. Wiedensohler, T. M. Tuch, D. S. Covert, P. Sheridan, J. A. Ogren, J. Gras, R. Nessler, C. Kleefeld, N. Kalivitis, et al. 2006. Intercomparisons and aerosol calibrations of 12 commercial integrating nephelometers of three manufacturers. *J. Atmos. Oceanic Technol.* 23 (7):902–14. doi:10.1175/JTECH1892.1.
- Hennigan, C. J., A. P. Sullivan, J. L. Collett, Jr., and A. L. Robinson. 2010. Levoglucosan stability in biomass burning particles exposed to hydroxyl radicals. *Geophys. Res. Lett.* 37 (9):L09806. doi:10.1029/2010GL043088.
- Jing, B., C. Peng, Y. Wang, Q. Liu, S. Tong, Y. Zhang, and M. Ge. 2017. Hygroscopic properties of potassium chloride and its internal mixtures with organic compounds relevant to biomass burning aerosol particles. *Sci. Rep.* 7:43572. doi:10.1038/srep43572.
- Kebabian, P. L., W. A. Robinson, and A. Freedman. 2007. Optical extinction monitor using cw cavity enhanced detection. *Rev. Sci. Instrum.* 78 (6):063102. doi:10.1063/1.2744223.
- Koehler, K., S. Kreidenweis, P. DeMott, A. Prenni, C. Carrico, B. Ervens, and G. Feingold. 2006. Water activity and activation diameters from hygroscopicity data. II. Application to organic species. *Atmos. Chem. Phys.* 6 (3):795–809. doi:10.5194/acp-6-795-2006.
- Lack, D. A., J. M. Langridge, R. Bahreini, C. D. Cappa, A. M. Middlebrook, and J. P. Schwarz. 2012. Brown carbon and internal mixing in biomass burning particles. *Proc Natl Acad Sci USA* 109 (37):14802–7. doi:10.1073/pnas.1206575109.
- Lack, D. A., E. R. Lovejoy, T. Baynard, A. Pettersson, and A. R. Ravishankara. 2006. Aerosol absorption measurement using photoacoustic spectroscopy: Sensitivity, calibration, and uncertainty developments. *Aerosol Sci. Technol.* 40 (9):697–708. doi:10.1080/02786820600803917.
- Langridge, J. M., M. S. Richardson, D. Lack, D. Law, and D. M. Murphy. 2011. Aircraft instrument for comprehensive characterization of aerosol optical properties. I. Wavelength-dependent optical extinction and its relative humidity dependence measured using cavity ringdown spectroscopy. *Aerosol Sci. Technol.* 45 (11):1305–18. doi:10.1080/02786826.2011.592745.
- Lee, A. K. Y., R. Zhao, R. Li, J. Liggio, S. M. Li, and J. P. D. Abbatt. 2013. Formation of light absorbing organo-nitrogen species from evaporation of droplets containing glyoxal and ammonium sulfate. *Environ. Sci. Technol.* 47 (22):12819–26. doi:10.1021/es402687w.
- Lee, J., M. Dubey, A. Aiken, P. Chylek, and C. Carrico. 2020. Optical and chemical analysis of absorption

- enhancement by mixed carbonaceous aerosols in the 2019 Woodbury, AZ, fire plume. *J. Geophys. Res. Atmos.* 125:e2020JD032399. doi:10.1029/2020JD032399.
- Lewis, K., W. Arnott, H. Moosmuller, R. Chakrabarty, C. Carrico, S. Kreidenweis, D. Day, W. Malm, A. Laskin, J. Jimenez, et al. 2009. Reduction in biomass burning aerosol light absorption upon humidification: Roles of inorganically-induced hygroscopicity, particle collapse, and photoacoustic heat and mass transfer. *Atmos. Chem. Phys.* 9 (22):8949–66. doi:10.5194/acp-9-8949-2009.
- Liu, F., D. R. Snelling, K. A. Thomson, and G. J. Smallwood. 2018. Estimate of scattering truncation in the cavity attenuated phase shift pmssa monitor using radiative transfer theory. *Aerosol Sci. Technol.* 52 (5):588–96. doi:10.1080/02786826.2018.1437891.
- Liu, J., M. Bergin, H. Guo, L. King, N. Kotra, E. Edgerton, and R. Weber. 2013. Size-resolved measurements of brown carbon in water and methanol extracts and estimates of their contribution to ambient fine-particle light absorption. *Atmos. Chem. Phys.* 13 (24):12389–404. doi:10.5194/acp-13-12389-2013.
- Lohmann, U., and J. Feichter. 2005. Global indirect aerosol effects: A review. *Atmos. Chem. Phys.* 5 (3):715–37. doi:10.5194/acp-5-715-2005.
- Malm, W., D. Day, S. Kreidenweis, J. Collett, C. Carrico, G. McMeeking, and T. Lee. 2005. Hygroscopic properties of an organic-laden aerosol. *Atmos. Environ.* 39 (27):4969–82. doi:10.1016/j.atmosenv.2005.05.014.
- Malm, W. C., and G. Persha. 1991. Considerations in the accuracy of a long-path transmissometer. *Aerosol Sci. Technol.* 14 (4):459–71. doi:10.1080/02786829108959506.
- Massoli, P., T. S. Bates, P. K. Quinn, D. A. Lack, T. Baynard, B. M. Lerner, S. C. Tucker, J. Brioude, A. Stohl, and E. J. Williams. 2009. Aerosol optical and hygroscopic properties during texaqs-gomaccs 2006 and their impact on aerosol direct radiative forcing. *J. Geophys. Res.* 114: D00F07. doi:10.1029/2008JD011604.
- Massoli, P., P. L. Keabian, T. B. Onasch, F. B. Hills, and A. Freedman. 2010. Aerosol light extinction measurements by cavity attenuated phase shift (caps) spectroscopy: Laboratory validation and field deployment of a compact aerosol particle extinction monitor. *Aerosol Sci. Technol.* 44 (6):428–35. doi:10.1080/02786821003716599.
- Matsui, H., D. S. Hamilton, and N. M. Mahowald. 2018. Black carbon radiative effects highly sensitive to emitted particle size when resolving mixing-state diversity. *Nat. Commun.* 9 (1):3446. doi:10.1038/s41467-018-05635-1.
- Michel Flores, J., R. Z. Bar-Or, N. Bluvshstein, A. Abo-Riziq, A. Kostinski, S. Borrmann, I. Koren, I. Koren, and Y. Rudich. 2012. Absorbing aerosols at high relative humidity: Linking hygroscopic growth to optical properties. *Atmos. Chem. Phys.* 12 (12):5511–21. doi:10.5194/acp-12-5511-2012.
- Mochida, M., and K. Kawamura. 2004. Hygroscopic properties of levoglucosan and related organic compounds characteristic to biomass burning aerosol particles. *J. Geophys. Res. Atmos.* 109:D21202. doi:10.1029/2004jd004962.
- Modini, R. L., J. C. Corbin, B. T. Brem, M. Irwin, M. Bertò, R. E. Pileci, P. Fetfatzis, K. Eleftheriadis, B. Henzing, M. M. Moerman, et al. 2020. Detailed characterization of the caps single scattering albedo monitor (caps pmssa) as a field-deployable instrument for measuring aerosol light absorption with the extinction-minus-scattering method. *Atmos. Meas. Tech. Discuss.* 14, 819–851, 2021 <https://doi.org/10.5194/amt-14-819-2021>.
- Onasch, T., P. Massoli, P. Keabian, F. Hills, F. Bacon, and A. Freedman. 2015. Single scattering albedo monitor for airborne particulates. *Aerosol Sci. Technol.* 49 (4):267–79. doi:10.1080/02786826.2015.1022248.
- Orozco, D., A. J. Beyersdorf, L. D. Ziemba, T. Berkoff, Q. Zhang, R. Delgado, C. J. Hennigan, K. L. Thornhill, D. E. Young, C. Parworth, et al. 2016. Hygroscopicity measurements of aerosol particles in the San Joaquin valley, ca, Baltimore, MD, and golden, co. *J. Geophys. Res. Atmos.* 121 (12):7344–59. doi:10.1002/2015JD023971.
- Parsons, M. T., D. A. Knopf, and A. K. Bertram. 2004. Deliquescence and crystallization of ammonium sulfate particles internally mixed with water-soluble organic compounds. *J. Phys. Chem. A* 108 (52):11600–8. doi:10.1021/jp0462862.
- Petters, M., and S. Kreidenweis. 2007. A single parameter representation of hygroscopic growth and cloud condensation nucleus activity. *Atmos. Chem. Phys.* 7 (8):1961–71. doi:10.5194/acp-7-1961-2007.
- Petzold, A., T. Onasch, P. Keabian, and A. Freedman. 2013. Intercomparison of a cavity attenuated phase shift-based extinction monitor (caps pmex) with an integrating nephelometer and a filter-based absorption monitor. *Atmos. Meas. Tech.* 6 (5):1141–51. doi:10.5194/amt-6-1141-2013.
- Quinn, P., T. Bates, T. Baynard, A. Clarke, T. Onasch, W. Wang, M. Rood, E. Andrews, J. Allan, C. Carrico, et al. 2005. Impact of particulate organic matter on the relative humidity dependence of light scattering: A simplified parameterization. *Geophys. Res. Lett.* 32 (22):L22809. doi:10.1029/2005GL024322.
- Romonosky, D., S. Gomez, J. Lam, C. Carrico, A. Aiken, P. Chylek, and M. Dubey. 2019. Optical properties of laboratory and ambient biomass burning aerosols: Elucidating black, brown, and organic carbon components and mixing regimes. *J. Geophys. Res. Atmos.* 124 (9):5088–105. doi:10.1029/2018JD029892.
- Russell, P., J. Redemann, B. Schmid, R. Bergstrom, J. Livingston, D. McIntosh, S. Ramirez, S. Hartley, P. Hobbs, P. Quinn, et al. 2002. Comparison of aerosol single scattering albedos derived by diverse techniques in two north Atlantic experiments. *J. Atmos. Sci.* 59 (3):609–19. > 2.0.CO₂. doi:10.1175/1520-0469(2002)059 < 0609:COASSA.
- Saleh, R., C. J. Hennigan, G. R. McMeeking, W. K. Chuang, E. S. Robinson, H. Coe, N. M. Donahue, and A. L. Robinson. 2013. Absorptivity of brown carbon in fresh and photo-chemically aged biomass-burning emissions. *Atmos. Chem. Phys.* 13 (15):7683–93. doi:10.5194/acp-13-7683-2013.
- Saleh, R., E. S. Robinson, D. S. Tkacik, A. T. Ahern, S. Liu, A. C. Aiken, R. C. Sullivan, A. A. Presto, M. K. Dubey, R. J. Yokelson, et al. 2014. Brownness of organics in aerosols from biomass burning linked to their black carbon content. *Nat. Geosci.* 7 (9):647–50. doi:10.1038/ngeo2220.
- Schkolnik, G., D. Chand, A. Hoffer, M. O. Andreae, C. Erlick, E. Swietlicki, and Y. Rudich. 2007. Constraining the density and complex refractive index of elemental and organic carbon in biomass burning aerosol using

- optical and chemical measurements. *Atmos. Environ.* 41 (5):1107–18. doi:10.1016/j.atmosenv.2006.09.035.
- Seinfeld, J. H., and S. N. Pandis. 1998. *Atmospheric chemistry and physics*. New York, USA: John Wiley and Sons, Inc.
- Singh, S., M. Fiddler, and S. Bilign. 2016. Measurement of size-dependent single scattering albedo of fresh biomass burning aerosols using the extinction-minus-scattering technique with a combination of cavity ring-down spectroscopy and nephelometry. *Atmos. Chem. Phys.* 16 (21): 13491–507. doi:10.5194/acp-16-13491-2016.
- Sullivan, A., A. Holden, L. Patterson, G. McMeeking, S. Kreidenweis, W. Malm, W. Hao, C. Wold, and J. Collett. 2008. A method for smoke marker measurements and its potential application for determining the contribution of biomass burning from wildfires and prescribed fires to ambient pm_{2.5} organic carbon. *J. Geophys. Res.* 113 (D22):D22302. doi:10.1029/2008JD010216.
- Sumlin, B. J., W. R. Heinson, and R. K. Chakrabarty. 2018. Retrieving the aerosol complex refractive index using pyMieScatt: A mie computational package with visualization capabilities. *J. Quant. Spectrosc. Radiat. Transf.* 205: 127–34. doi:10.1016/j.jqsrt.2017.10.012.
- Tan, H., H. Xu, Q. Wan, F. Li, X. Deng, P. W. Chan, D. Xia, and Y. Yin. 2013. Design and application of an unattended multifunctional h-tdma system. *J. Atmos. Oceanic Technol.* 30 (6):1136–48. doi:10.1175/JTECH-D-12-00129.1.
- Tang, M., C. Chan, Y. Li, H. Su, Q. Ma, Z. Wu, G. Zhang, Z. Wang, M. Ge, M. Hu, et al. 2019. A review of experimental techniques for aerosol hygroscopicity studies. *Atmos. Chem. Phys.* 19 (19):12631–86. doi:10.5194/acp-19-12631-2019.
- Teich, M., D. van Pinxteren, M. Wang, S. Kecorius, Z. Wang, T. Müller, G. Močnik, and H. Herrmann. 2017. Contributions of nitrated aromatic compounds to the light absorption of water-soluble and particulate brown carbon in different atmospheric environments in Germany and China. *Atmos. Chem. Phys.* 17 (3):1653–72. doi:10.5194/acp-17-1653-2017.
- Wang, Y., P.-L. Ma, J. Peng, R. Zhang, J. H. Jiang, R. C. Easter, and Y. L. Yung. 2018. Constraining aging processes of black carbon in the community atmosphere model using environmental chamber measurements. *J. Adv. Model. Earth Syst.* 10 (10):2514–26. doi:10.1029/2018MS001387.
- Ward, T. J., R. F. Hamilton, Jr., R. W. Dixon, M. Paulsen, and C. D. Simpson. 2006. Characterization and evaluation of smoke tracers in pm: Results from the 2003 Montana wildfire season. *Atmos. Environ.* 40 (36): 7005–17. doi:10.1016/j.atmosenv.2006.06.034.
- Washenfelder, R., J. Flores, C. Brock, S. Brown, and Y. Rudich. 2013. Broadband measurements of aerosol extinction in the ultraviolet spectral region. *Atmos. Meas. Tech.* 6 (4):861–77. doi:10.5194/amt-6-861-2013.
- Washenfelder, R. A., A. R. Attwood, C. A. Brock, H. Guo, L. Xu, R. J. Weber, N. L. Ng, H. M. Allen, B. R. Ayres, K. Baumann, et al. 2015. Biomass burning dominates brown carbon absorption in the rural southeastern United States. *Geophys. Res. Lett.* 42 (2):653–64. doi:10.1002/2014GL062444.
- Xu, L., and J. E. Penner. 2012. Global simulations of nitrate and ammonium aerosols and their radiative effects. *Atmos. Chem. Phys.* 12 (20):9479–504. doi:10.5194/acp-12-9479-2012.
- Ye, X., T. Chen, D. Hu, X. Yang, J. Chen, R. Zhang, A. F. Khakuziv, and L. Wang. 2009. A multifunctional htdma system with a robust temperature control. *Adv. Atmos. Sci.* 26 (6):1235–40. doi:10.1007/s00376-009-8134-3.
- Yu, H., Y. J. Kaufman, M. Chin, G. Feingold, L. A. Remer, T. L. Anderson, Y. Balkanski, N. Bellouin, O. Boucher, S. Christopher, et al. 2006. A review of measurement-based assessments of the aerosol direct radiative effect and forcing. *Atmos. Chem. Phys.* 6 (3):613–66. doi:10.5194/acp-6-613-2006.
- Zhang, F., Y. Wang, J. Peng, L. Chen, Y. Sun, L. Duan, X. Ge, Y. Li, J. Zhao, C. Liu, et al. 2020. An unexpected catalyst dominates formation and radiative forcing of regional haze. *Proc. Natl. Acad. Sci. U.S.A.* 117 (8): 3960–6. doi:10.1073/pnas.1919343117.
- Zhao, W., X. Xu, B. Fang, Q. Zhang, X. Qian, S. Wang, P. Liu, W. Zhang, Z. Wang, D. Liu, et al. 2017. Development of an incoherent broad-band cavity-enhanced aerosol extinction spectrometer and its application to measurement of aerosol optical hygroscopicity. *Appl. Opt.* 56 (11):E16–E22. doi:10.1364/AO.56.000E16.
- Zhou, H.-B., J. Shao, H.-G. Qian, C.-F. Ying, and Y.-B. Zhang. 2019. A novel analytical method of time-dependent absorption spectroscopy. *Spectrosc. Spectral Anal.* 39: 673–8. doi:10.3964/j.issn.1000-0593(2019)03-0673-06.
- Zhou, J., X. Xu, W. Zhao, B. Fang, Q. Liu, Y. Cai, W. Zhang, D. Venables, and W. Chen. 2020. Simultaneous measurements of the relative-humidity-dependent aerosol light extinction, scattering, absorption, and single-scattering albedo with a humidified cavity-enhanced albedometer. *Atmos. Meas. Tech.* 13 (5):2623–34. doi:10.5194/amt-13-2623-2020.